

# PRECISION MEASUREMENTS OF $^{20}\text{F}$ BETA DECAY

By

Maximilian Nathan Hughes

A DISSERTATION

Submitted to  
Michigan State University  
in partial fulfillment of the requirements  
for the degree of

2019

# ABSTRACT

PRECISION MEASUREMENTS OF  $^{20}\text{F}$  BETA DECAY

By

Maximilian Nathan Hughes



## ACKNOWLEDGMENTS

# TABLE OF CONTENTS

|   |             |
|---|-------------|
| <b>LIST OF TABLES . . . . .</b>   | <b>vii</b>  |
| <b>LIST OF FIGURES . . . . .</b>  | <b>viii</b> |
| <b>Chapter 1 Introduction . . . . .</b>                                   | <b>1</b>    |
| 1.1 Beta Decay . . . . .  | 1           |
| <b>Chapter 2 Theoretical Description of Beta Decay Spectrum . . . . .</b> | <b>2</b>    |
| 2.1 Phase Space Beta Decay . . . . .                                      | 3           |
| 2.1.1 Matrix Elements . . . . .   | 5           |
| 2.2 Variables of Correction Formula . . . . .                             | 5           |
| 2.3 Fermi Function . . . . .  | 7           |
| 2.4 Radiative Correction . . . . .  | 7           |
| 2.4.1 Inner Bremsstrahlung . . . . .                                      | 8           |
| 2.5 Screening . . . . .   | 10          |
| 2.5.1 Potentials Used in Screening Derivation . . . . .                   | 11          |
| 2.5.2 Screening Correction Formula . . . . .                              | 13          |
| <b>Chapter 3 <math>^{20}\text{F}</math> . . . . .</b>                     | <b>14</b>   |
| 3.1 Theory Parameters . . . . .   | 15          |
| <b>Chapter 4 Experimental Description . . . . .</b>                       | <b>16</b>   |
| 4.1 Experimental technique . . . . .                                      | 16          |
| 4.2 Creating $^{20}\text{F}$ Beam . . . . .                               | 17          |
| 4.2.1 Beam Size and Location . . . . .                                    | 18          |
| 4.2.2 Beam Purity . . . . .   | 19          |
| 4.3 Detector Set Up . . . . .   | 20          |
| 4.3.1 $^{20}\text{F}$ Decay Detectors . . . . .                           | 20          |
| 4.3.2 Other detectors . . . . .   | 22          |
| 4.3.3 Powering the Detectors . . . . .                                    | 22          |
| 4.3.4 Verifcation of Implant Depth . . . . .                              | 23          |
| 4.4 Experimental Conditions . . . . .                                     | 24          |
| <b>Chapter 5 Data Processing . . . . .</b>                                | <b>25</b>   |
| 5.1 Data acquisiton . . . . .   | 25          |
| 5.1.1 Data Acquisition Software . . . . .                                 | 26          |
| 5.2 Data Taking and Processing . . . . .                                  | 27          |
| <b>Chapter 6 Half Life Measurement . . . . .</b>                          | <b>28</b>   |
| 6.1 Motivation . . . . .  | 28          |
| 6.2 Half life data analysis . . . . .                                     | 29          |

|                     |  |           |
|---------------------|--|-----------|
| 6.2.1               | Data Selection . . . . .                           | 29        |
| 6.2.2               | Cut Selection . . . . .                            | 31        |
| 6.3                 | Systematic Effects . . . . .                       | 38        |
| 6.3.1               | Dead Time . . . . .                                | 38        |
| 6.3.2               | Pile Up Effects . . . . .                          | 38        |
| 6.3.3               | Background . . . . .                               | 39        |
|                     | 6.3.3.1 Simultaneous vs Seperate Fitting . . . . . | 40        |
|                     | 6.3.3.2 Spectra Arguments . . . . .                | 41        |
| 6.3.4               | Cut Sensitivity . . . . .                          | 42        |
| 6.3.5               | Oscillator Stability . . . . .                     | 42        |
| 6.3.6               | Binning and Fitting . . . . .                      | 43        |
| 6.4                 | Result and discussion . . . . .                    | 43        |
| 6.5                 | Conclusion . . . . .                               | 44        |
| <b>Chapter 7</b>    | <b>Fitting Beta Spectrum . . . . .</b>             | <b>46</b> |
| 7.1                 | GEANT4 Monte Carlo . . . . .                       | 46        |
| 7.1.1               | Detector Simulation . . . . .                      | 46        |
| 7.1.2               | Source Definition . . . . .                        | 47        |
| 7.1.3               | Primary Particle Definitions . . . . .             | 47        |
| 7.1.4               | Simulation Results Processing . . . . .            | 49        |
| 7.2                 | Calibration . . . . .                              | 50        |
| 7.3                 | Fitting Procedure . . . . .                        | 50        |
| <b>BIBLIOGRAPHY</b> | <b>. . . . .</b>                                   | <b>52</b> |

## LIST OF TABLES

|   |    |
|---|----|
| Table 2.1: Variables used in the theory corrections . . . . . | 5  |
| Table 6.1: The PVT runs . . . . .                             | 30 |
| Table 6.2: The PVT runs . . . . .                             | 43 |
| Table 6.3: Systematics . . . . .                              | 44 |

## LIST OF FIGURES

|             |  |    |
|-------------|--|----|
| Figure 2.1: | An estimate of the theory uncertainty due to the experimental parameter uncertainty. Shown are the slopes for each experimental parameter. They are orders of magnitude smaller than the $10^{-2}/\text{MeV}$ of the $C_1$ . . . . .                 | 6  |
| Figure 2.2: | Comparing three different radiative corrections. The green line depends strongly on the detector geometry . . . . .  | 10 |
| Figure 2.3: | Starting all three radiative corrections from the same place. The green line is about halfway between the two others. . . . .  | 11 |
| Figure 3.1: | The decay scheme of $^{20}\text{F}$ . . . . .  | 14 |
| Figure 4.1: | The beam spot of the calibrated PPAC spectrum. The samples of the spectrum that were averaged together are shown in the black dots. The center of the fit is not shown. . . . .  | 19 |
| Figure 4.2: | A sketch of the detector set up. Shown here is with the PVT detector implant. The CsI (Na) detector was centered in the middle of the the four gamma detectors and recessed by 1 inch. The bottom image shows a side of the detector set-up. . . . . | 21 |
| Figure 6.1: | Previous measurements of the $^{20}\text{F}$ half-life. The labels correspond to: Mal [10], Gli [7], Yul [21], Wil [18], Alb [1], Gen [6], Min [11], Wan [16] and Ito [8]. . . . .   | 28 |
| Figure 6.2: | The effect of the lower beta cut vs the half-life in the CsI(Na) data . . .  | 29 |
| Figure 6.3: | The light pulse as a function of time for set 1. The gain changes smoothly over time. This causes a large change in the half-life as the beta cuts are moved. . . . .  | 31 |
| Figure 6.4: | The 511 region can be seen in this graph . . . . .   | 32 |
| Figure 6.5: | The lower beta cut was selected to be above the 511 region. The upper beta cut was selected to include all the pile up . . . . .   | 32 |
| Figure 6.6: | The wide cuts are to reduce the effect of the rate dependent gain. . . . .   | 33 |



|              |  |    |
|--------------|--|----|
| Figure 6.7:  | This is a gamma and beta energy filtered spectrum of the time difference between the up detector and the PVT implant detector. The tail on the right side of the large peak is due to pile up. The narrow time cuts are shown with a dotted line. The wide time cuts are shown with a solid line.  | 34 |
| Figure 6.8:  | A sketch of the pile up events. A $^{20}\text{F}$ decay happens at time = t1. The green electron is detected in the implant detector. The black arrow (the gamma ray) is not. Then, later at time = t2, another $^{20}\text{F}$ decays. t2 is within the pile-up window of t1. Both electrons energies pile-up and are added together. However, the time stamp recorded by the DAQ is still t1. The gamma ray from event t2 can be detected in a gamma detector at time t2. This creates the uncorrelated event pedestal in the time difference graph. | 35 |
| Figure 6.9:  | The time difference spectrum zoomed out. This figure is shown with energy coincidences.  | 36 |
| Figure 6.10: | The decay spectrum from the up gamma detector is shown on the top graph. The red line is the exponential fit. The bottom graph shows the residuals from the fit.   | 37 |
| Figure 6.11: | Time difference vs the resulting half-life. The line is a quadratic fit which was extrapolated to zero.  | 39 |
| Figure 6.12: | The red lines show the results of the fits over the runs that were used. The additional half-lives shown are excluded to reasons discussed previously.   | 44 |
| Figure 6.13: | A scatter plot of (a) previous values with this work added. The labels correspond to: Mal [10], Gli [7], Yul [21], Wil [18], Alb [1], Gen [6], Min [11], Wan [16] and Ito [8].   | 45 |

# Chapter 1

## Introduction

Precision measurements at low energy can compete with high energy measurements.

### 1.1 Beta Decay

Beta decay is cool and good.

# Chapter 2

## Theoretical Description of Beta Decay Spectrum

To obtain a measure of the Fierz term, the beta decay spectrum must be precisely described. The description of the beta decay spectrum is written as a series of corrections on top of the main phase space factor.

The corrections depend on several parameters of the decay. Some of them are just numbers, such as the atomic number of the daughter or mother nucleus or the mass number of the system. However, there are two important parameters that are inexact. They are measured experimentally.

One is the  $Q$ -value of the decay, which is defined in equation 3.1.

$$Q = m_p - (m_d + E_\gamma) \tag{2.1}$$

where  $Q$  is the  $Q$ -value,  $m_p$  is the mass of the parent nucleus,  $m_d$  is the mass of the daughter nucleus, and  $E_\gamma$  is the energy of any gamma rays in the decay. For this measurement, the atomic mass of  $^{20}\text{Ne}$  and  $^{20}\text{F}$  were used [12]. The mass of the electrons subtracts out atomic masses, since in neutral fluorine there are nine electrons, and one electron is gained from the beta decay. This then equals the ten electrons in the atomic mass of neon. The only correction missing is the small, eV scale electron binding energy of the last electron.

The other parameter is the charge radius of the daughter nucleus. There are several ways to calculate the charge radius. In this work, the charge radius was taken from the measured RMS charge radius and converted. It was assumed that the  $^{20}\text{Ne}$  nucleus was a sphere. From this, the radius was calculated using equation 2.2

$$r = \sqrt{\frac{5}{3}} r_{rms} \quad (2.2)$$

where  $r_{rms}$  is the root mean square radius, and  $r$  the charge radius.

With the two parameters, the q-value and the phase space, the shape of all beta decay spectra can be described.

## 2.1 Phase Space Beta Decay

The main part of the beta decay spectrum is the phase space factor. It is shown in equation 2.3

$$\frac{dN}{dE} = C * p_{\beta} W (Q - W)^2 \quad (2.3)$$

where  $C$  is a constant which includes the matrix element squared,  $p_{\beta}$  is the beta momentum,  $W$  the total electron energy, and  $Q$  the q-value of the beta decay. This is derived from the density of states of the particle. This comes in from Fermi's Golden Rule, which is shown in equation 2.4.

$$\lambda = \frac{2\pi}{\hbar} \|M\|^2 \rho \quad (2.4)$$

where  $\lambda$  is the transition probability,  $M$  the matrix element, and  $\rho$  the density of the

states. The main effect on the spectrum shape originates from the density of states. The number of states for both the electron and the neutrino is show in equation 2.5

$$N = \frac{1}{(2\pi\hbar)^6} \int dr_\beta^3 \int dp_\beta^3 \int dr_{\nu_e}^3 \int dp_{\nu_e}^3 \quad (2.5)$$

where  $r$  and  $p$  corresponds to the position and momentum of the electron ( $\beta$ ) and the neutrino ( $\nu_e$ ). Doing the integral over both  $r$ 's give two factors of the volume, which disappear when the next factor is introduced. Since the neutrinos are unmeasured, the momentum of the neutrinos is integrated over. Assuming spherical symmetry, the new integral is shown in equation 2.6

$$dN = \frac{V^2}{4\pi^4\hbar^6} p_\beta^2 dp_\beta p_{\nu_e}^2 dp_{\nu_e} \quad (2.6)$$

This is simplified by approximating the neutrino as massless. The momentum of the neutrino is then equal to the energy of the neutrino. Then, the total energy  $E$  is written as a sum of the neutrino energy (or momemntum) and the beta energy. Plugging that in gives equation 2.7 after integrating over the neutrino degrees of freedom.

$$dN = \frac{V^2}{4\pi^4\hbar^6} (E - E_{beta})^2 p_\beta^2 dp_\beta \quad (2.7)$$

Then, the only thing left to do to recover equation 2.3 is to rewrite  $dp$  in terms of  $dE$ . The energy  $E_{beta}$  has been replaced with  $W$ , which is the energy of the electron divided by the mass an electron, and  $E$  has been replaced by the Q-value. Since the measurement is not an absolute one, but only concerned with the shape of the spectrum, the normalization factor is arbitrary.

This is the main factor in describing the beta decay energy spectrum.

### 2.1.1 Matrix Elements

In the above discussion, the matrix elements of the beta decay was glossed over.

INSERT DISCUSSION HERE

## 2.2 Variables of Correction Formula

For the rest of the discussion on beta decay corrections, everything is given without units.

All of the energies are divided by the electron mass, i.e. 511 keV. The other important variables are shown in table 2.1

Table 2.1: Variables used in the theory corrections

| Variable | Description                                | Equation or Value                             |
|----------|--|---|
| $A$      | Mass number                                | 20  |
| $Z$      | Atomic number of daughter                  | 10  |
| $\alpha$ | Fine structure constant                    | 1/137.0359                                    |
| $R$      | Root mean square charge radius of daughter | 3.055 fm [2]                                  |
| $W$      | Total energy of beta electron              | $E/m_e$                                       |
| $p$      | Electron momentum                          | $\sqrt{W^2 - 1}$                              |
| $W_0$    | Maximum electron energy                    | $\frac{M_{20F} - M_{20Ne} - E_{\gamma}}{m_e}$ |
| $\gamma$ | Factor that shows up in EM corrections     | $\sqrt{1 - (\alpha Z)^2}$                     |

To convert the RMS charge radius into the regular charge radius, it is assumed that the nucleus was a sphere. This means multiplying the radius given in table 2.1 by  $\sqrt{\frac{3}{5}}$ . Finally, in order to put it into natural units, the result was divided by the reduced Compton wavelength of the electron.

The two factors that require experimental input were  $R$  and  $E_0$ .  $R$  was given directly in data tables. For  $E_0$ , the mass of  $^{20}\text{F}$  and  $^{20}\text{Ne}$  were needed. The energy of the gamma ray

photon was also needed. Each one of these had an uncertainty, which propagates through the various correction functions. Before the theoretical corrections were fed into a Monte Carlo simulation, the uncertainties were checked. Theoretical spectra were built with each value plus or minus its uncertainty. Ratios between the spectra were taken and fit with a line. The results of those ratios are seen in figure 2.1.

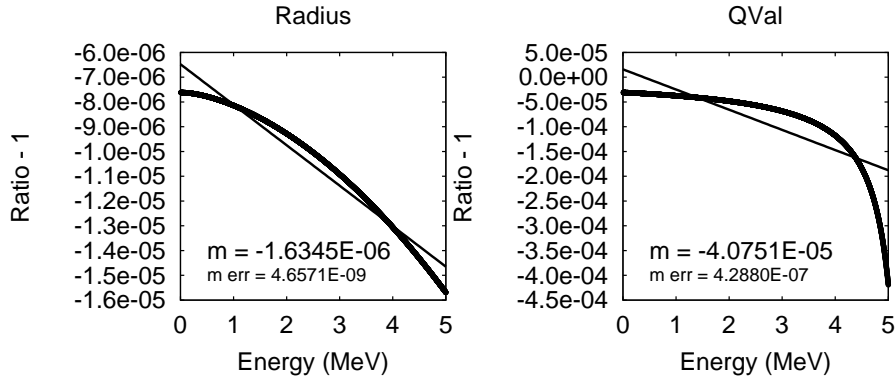


Figure 2.1: An estimate of the theory uncertainty due to the experimental parameter uncertainty. Shown are the slopes for each experimental parameter. They are orders of magnitude smaller than the  $10^{-2}/\text{MeV}$  of the  $C_1$ .

Since the slopes of each line are much smaller than the shape factor values, the experimental uncertainties are negligible. The various theoretical corrections that are needed are now discussed below.

## 2.3 Fermi Function

The largest correction. This accounts for the interaction of the charge of the outgoing electron and the charge of the nucleus. It is calculated by taking the Dirac equation wave functions and assuming the nucleus is a point charge of  $Ze$ . The Dirac wave functions are taken down to a nuclear radius  $R$ . This is since the wave functions diverge [19].

The Fermi function is printed in equation 2.8

$$F(Z, W) = 2 \frac{\gamma + 1}{\Gamma(2\gamma + 1)^2} (2pR)^{2(\gamma-1)} e^{\frac{\pi\alpha ZW}{p}} \left\| \Gamma(\gamma + i \frac{\alpha ZW}{p}) \right\|^2 \quad (2.8)$$

While this is the largest correction, it is the most understood one. It also only depends on one parameter with experimental uncertainty,  $R$ .

## 2.4 Radiative Correction

The radiative correction was the next largest correction. For this measurement, the correction is only need to first order, which is on order  $\alpha$ . The correction is a QED correction that stems from photons emitted from the beta particle. This photon can be absorbed by the nucleus of the daughter, which makes it a virtual photon. The photon can also be a real photon that propogates out off to inifinity. The real photons are known as inner bremsstrahlung.

There are different descriptions of the radiative correction. The first is by Sirlin [13] and is shown in equation 2.9.

$$R(W, W_0) = 1 + \frac{\alpha}{2\pi} [3\ln(M) - \frac{3}{4} + 4(\frac{\text{arctanh}(\beta)}{\beta} - 1) * (\frac{W_0 - W}{3W} - \frac{3}{2} + \ln(2(W_0 - W))) + \frac{4}{\beta} L(\frac{2\beta}{1+\beta}) + \frac{\text{arctanh}(\beta)}{\beta} * (2 * (1 + \beta^2) + \frac{(W_0 - W)^2}{6W^2} - 4\text{arctanh}(\beta))] \quad (2.9)$$



with  $\beta = \frac{p}{W}$ ,  $M$  the proton mass, and  $L(\frac{2\beta}{1+\beta})$  refering to the Spence function, as seen in equation 2.10 [20]

$$L(x) = \int_0^x \frac{\ln(1-t)}{t} dt \quad (2.10)$$

The Sirlin formula assumes that the inner bremsstrahlung photons are not detected at all. This is mostly true if the source of the beta decay is centered outside of a detector. However, if the source is implanted inside of the detector, such as it is in this experiment, some of the inner bremsstrahlung is absorbed.

If it is all absorbed, a different form of the first order radiative correction is needed. There are many equivalent forms of this, but the one that was used for this experiment was by Fayans [5]. The form of this radiative correction is shown in equation 2.11

$$R(W, W_0) = 1 + \frac{\alpha}{\pi} [(\frac{2}{\beta} \ln(\frac{2\beta}{1+\beta}) + \frac{7}{8\beta} + \frac{3\beta}{8}) \ln(\frac{1+\beta}{1-\beta}) - 2 \ln(\frac{4\beta^2}{1-\beta^2}) + \frac{4}{\beta} L(\frac{2\beta}{1+\beta}) + \frac{23}{8} + \frac{3}{2} \ln(M)] \quad (2.11)$$

With all the functions and variables meaning the same as in equation 2.9.

Unfortunately, the amount of inner bremsstrahlung absorbed depends on the geometry. A more careful treatment of the radiative correction was used.

### 2.4.1 Inner Bremsstrahlung

To first order, the energy spectrum of the inner bremsstrahlung photons is independent of  $Z$ . This is exactly like the two radiative corrections shown in equations 2.9 and 2.11. The spectrum is written out in equation 2.12 [9]

$$\Phi(k, W_e) = \frac{\alpha p}{\pi p_e k} \left( \frac{W_e^2 + W^2}{W_e p} \log(W + p) - 2 \right) \quad (2.12)$$

where  $\Phi(k, W_e)$  is the probability density of seeing a photon of energy  $k$  from an electron of initial energy  $W_e$ . This equation was derived one way using outgoing waves from the Dirac equation in polar coordinates. The first order Born approximations was used. This means that at low energies, equation 2.12 is inaccurate. That can be seen, as the equation diverges as  $k$  goes to zero. If more orders of the approximation are added, this divergence can be controlled. These higher orders would correspond to emitting multiple photons. Each of these orders would have a probability reduced by a factor of  $\alpha$  compared to equation 2.12. The higher orders would be less significant, expect for at low energies. Since the probability density diverges, the higher orders could contribute. This would make the probability of emitting no photons finite.

However, another possibility is to add a cutoff. As long as the cutoff is high enough to be in the region where the first order Born approximation is valid, but low enough not to cut out gamma rays that are not full absorbed, equation 2.12 is usable. The cutoff used was 50 keV. This cutoff was checked using Monte Carlo, and is within the region where the detector and the source geometry absorbs all gamma rays.

To quantify the exact effect of the inner bremsstrahlung, a GEANT4 simulation was used. Electrons were generated using the phase space and the radiative correction in equation 2.11. Then, for each electron, equation 2.12 was sampled and a photon generated. No other physics process was looked at in this simulation. The ratio consisting of the energy absorbed over the initial energy was the output of the simulation. That ratio is the effective efficiency of absorbing the inner bremsstrahlung photons. Multiplying that ratio by equation 2.11 gives

the effective radiative correction. Comparing all three radiative corrections can be seen in figure 2.2

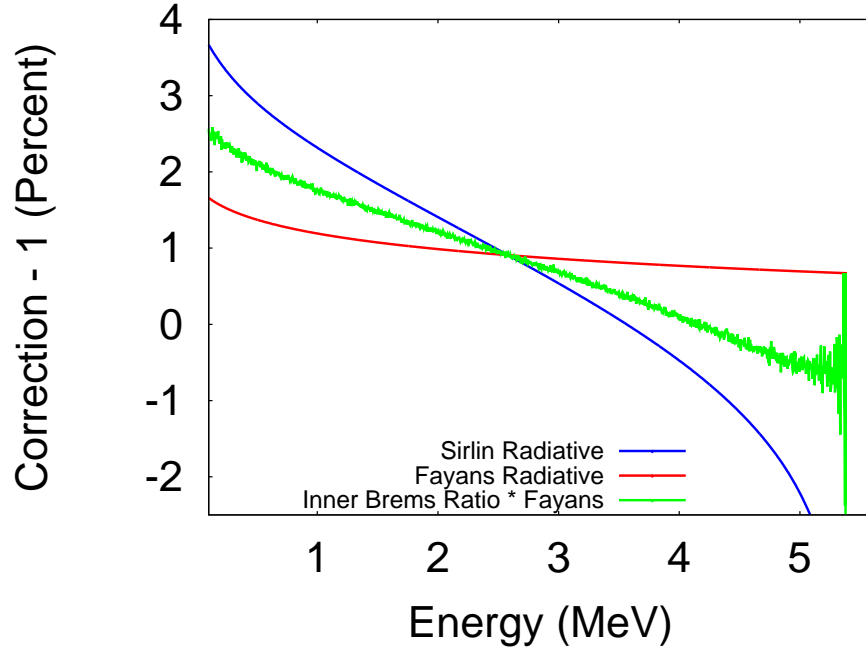


Figure 2.2: Comparing three different radiative corrections. The green line depends strongly on the detector geometry

In order to see the effect of each correction on the slope, all three corrections offset in order to start from the same starting point. This is seen in figure 2.3. The effect of the inner bremsstrahlung is to put the radiative correction halfway between the Sirlin and the Fayans formulas.

## 2.5 Screening

The screening correction is the next largest correction. It corresponds to the screening of the nuclear charge due to the electron cloud of the atom. The strongest effect of the screening correction is at low electron energies. This is a correction to the Fermi function.

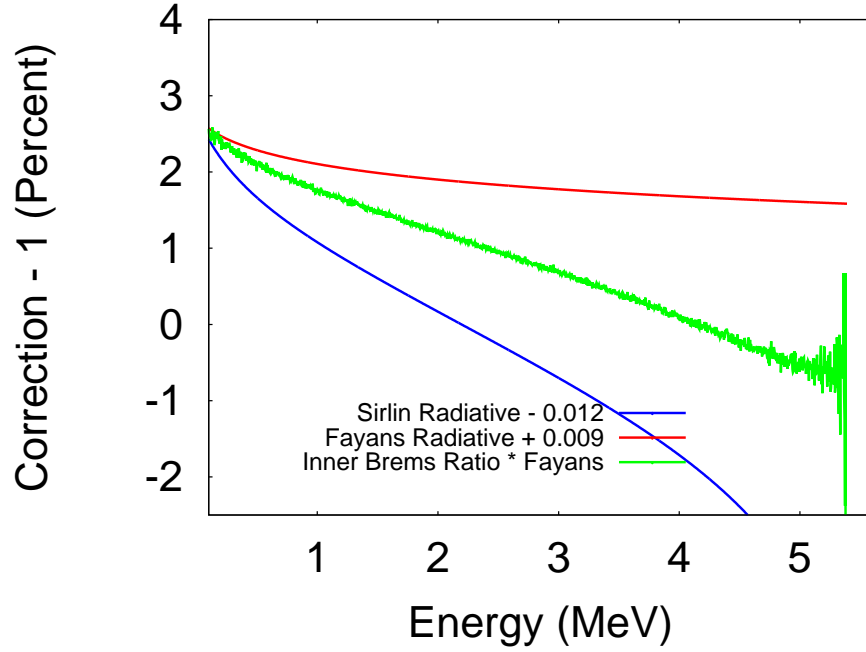


Figure 2.3: Starting all three radiative corrections from the same place. The green line is about halfway between the two others.

### 2.5.1 Potentials Used in Screening Derivation

To calculate this correction, the Coulomb potential used to calculate the Fermi function is replaced with a Hulthén potential. This is shown in equation 2.13

$$V(r) = -\frac{\alpha Z \beta}{e^{\beta r} - 1} \quad (2.13)$$

Where  $r$  is the distance away from the center and  $\beta$  is a parameter characterizing the defuseness of the electron cloud. The ratio of this new Fermi function to the old Fermi function is the screening correction. It multiplies the phase space.

The screening correction is negligible except for near the origin. Near the origin, equation 2.13 behaves as equation 2.14

$$V(r) = -\frac{\alpha Z}{r} + \frac{1}{2}\alpha Z\beta \quad (2.14)$$

and  $\beta$  is given by equation 2.15 [4].

$$\beta = 2C(Z)\alpha Z^{\frac{1}{3}}m_e \quad (2.15)$$

In the case of beta decay, the  $Z$  is number electrons of the mother atom. The assumption is that beta decay is occurring from neutral mother atoms. The only unknown is  $C(Z)$ .

To find the value of  $C(Z)$ , a comparison to another method of treating screening is needed. In another method of describing screening, the potential is described as a series of exponentials. This is shown in 2.16 [3].

$$V(r) = -\frac{\alpha Z}{r} \sum_n c_n e^{-b_n x} \quad (2.16)$$

where  $b_n$  and  $c_n$  are constants. The sum of all the  $c_n$  adds up to one. The value of  $x$  is shown in equation 2.17 [3]

$$x = 1.13\alpha Z^{\frac{1}{3}}r m_e \quad (2.17)$$

When equation 2.16 is expanded near the origin, the result is equation 2.18

$$V(r) = -\frac{\alpha Z}{r} + \alpha Z 1.13\alpha Z^{\frac{1}{3}}m_e \sum_n b_n c_n \quad (2.18)$$

By comparing equation 2.14, equation 2.15 and equation 2.18, the results in equation 2.19 are obtained.

$$C(Z) = 1.13 \sum_n c_n b_n \tag{2.19}$$

For fluorine,  $n = 1$ ,  $c = 1$ , and  $b = 0.907$  [3].

### 2.5.2 Screening Correction Formula

With all these factors out of the way, the screening correction can be written. The formulas in the

# Chapter 3

## $^{20}\text{F}$

In this measurement, the nucleus used was  $^{20}\text{F}$ . The decay scheme is given in figure 3.1.

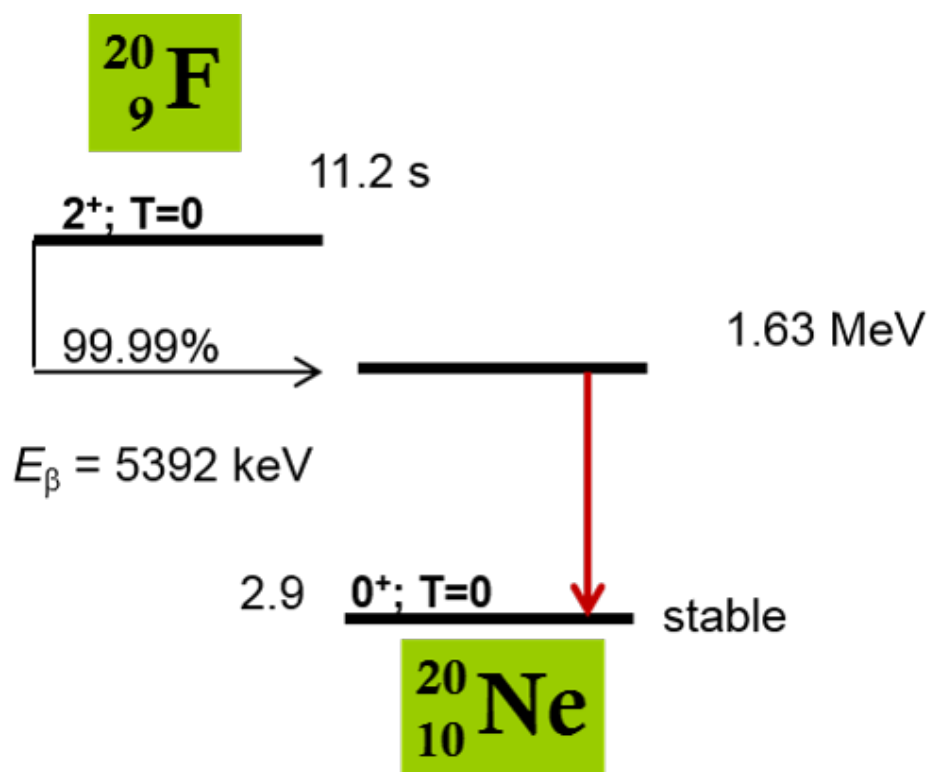


Figure 3.1: The decay scheme of  $^{20}\text{F}$ .

As seen in the figure,  $^{20}\text{F}$  decays 99.999% of the time to the first excited state of  $^{20}\text{Ne}$ . The  $2^+$  state seen in the decay scheme is not the isobaric analogue state to the ground state of  $^{20}\text{F}$ . That state is much higher in energy. The beta decay therefore has a isospin change of 1, and is a Gamow-Teller transition. Given the discussion in the previous chapter, it means that any Fierz term measured in this decay would be sensitive to a tensor coupling in the

weak force.

### 3.1 Theory Parameters

For the q-value of the decay, the atomic masses of  $^{20}\text{Ne}$  and  $^{20}\text{F}$  were used. The decay of  $^{20}\text{F}$  of interest decays to an excited state of the  $^{20}\text{Ne}$ . The energy of the gamma ray was measured to 0.015 keV [14].

Using the numbers described above and equation 3.1, the q-value for  $^{20}\text{F}$  is 5.901928 (82). The largest source of uncertainty is in the mass of  $^{20}\text{F}$ .

$$Q = m_{20F} - (m_{20Na} + E_\gamma) \tag{3.1}$$



# Chapter 4

## Experimental Description

The experiment was run at the National Superconducting Cyclotron Laboratory (NSCL) in East Lansing, Michigan. The experiment was run from September 1, 2015 to September 7, 2015.

### 4.1 Experimental technique

The technique used was a calorimetric technique. This reduced several effects could otherwise distort the beta decay spectrum. The largest of these is backscattering. If a beta decay source is placed outside a scintillator, there is a chance that the electrons will go into the scintillator and bounce back out. This happens in the surface of the detector, and therefor the electron deposits very little energy into the detector. The disortion of backscattering is most at low energies. Beta decay electrons can also scatter out of the detector to the sides as well. This also distorts the beta spectrum. Lastly if there is a dead layer at the surface of the crystal, the energy depositted in that layer will not be absorbed.

With the calorimetric technique, the radioactive nucleus is surrounded by scintillator material. As long as the nuclei are implanted deep enough, the electrons will not have enough energy to escape the detector. Even if the electron scatters several times, it still deposits all it's energy. This range depends on the detector material. Since any dead layers are at the surface, the decays inside the detector do not see them. A  $4\pi$  angular coverage is

also obtained, as the detector material surrounds the source.

There are some caveats for a calorimetric technique. The first is that the electrons moving through the scintillator material will emit a lot of bremsstrahlung. Using a low-Z detector material will lessen this effect. The machines used to generate the isotope of interest must be able to create them at high enough energy in order to implant the isotopes deep enough into your detector. This limits what nuclei can be used for this technique. The act of implanting the nuclei creates a lot of light. The beam used needs to be allowed to implant, and then allowed to decay over some time.

For this experiment, a beam of  $^{20}\text{F}$ , was implanted into two different detectors. Two different detectors were used to cross-check different systematics. After an amount of  $^{20}\text{F}$  was implanted, the beam was turned off by dephasing the cyclotrons. Then, the  $^{20}\text{F}$  was allowed to decay inside the detector. Given the half-life of  $^{20}\text{F}$  of 11 s, the decay time was varied between 22 and 60 s.

## 4.2 Creating $^{20}\text{F}$ Beam

The primary beam of  $^{22}\text{Ne}$  was accelerated by the coupled cyclotrons to 150 MeV/A. A typical intensity of the primary beam was around  $60 * 10^{-5}\text{pnA}$ . It was impinged on a Be target and sent through the fragment separator. The resulting  $^{20}\text{F}$  beam was at an energy of 130 MeV/A. The intensity of the  $^{20}\text{F}$  was about  $2 * 10^{-5}\text{pnA}$ , and the purity was about 93% at the end of the fragment separator.

To measure the  $^{20}\text{F}$  beta decay spectrum, a beam of  $^{20}\text{F}$  was implanted into one of two different detectors. The isotope was implanted deeply enough from so that the detector material could completely absorb the energy of electron at the end point energy. The implan-

tation of the beam was done to avoid instrumental effects of a non-calorimetry experiment. If there is a dead layer, there is more detector behind the layer to absorb the energy. The electron cannot scatter out of the detector.

#### **4.2.1 Beam Size and Location**

To test the size of the beam, a parallel plate avalanche counter was used. The size of the detector was 10 cm by 10 cm square. It was placed 65 cm upstream of the target. A horizontal and vertical grid was in the detector. Depending on where on each of the grids the particles hit, different charges were sent to either end of the PPAC. The signals were fed into a digital data acquisition system, and read out as an energy. The difference of the two signals divided by the sum was interpreted as a position.

To calibrate the detector, a mask with several holes was used. This mask covered the front of the detector, and an alpha source in the vacuum was placed in front of the PPAC. Then, everything was left to run until an image of the mask was formed. The mask had holes in it every 1 cm. It also had a large L shaped hole so that the orientation of the mask could be seen. With this, the PPAC could be calibrated.

Before taking data for the beta decay spectrum measurement, the PPAC was inserted into the beam. After adjusting the parameters of the upstream beam optics, the final beam size at the PPAC was measured. The calibrated data of the signals was built into a 3-D histogram. There was some ringing in the PPAC, so the peak of the beam spot was fitted with a 3-D gaussian function. The average of the gaussian and the sigma in the x and y direction was taken. From the sigmas, the half widths at half maximum (HWHM) in both directions were calculated. The distribution of the locations were sampled at eight different points. The points are shown as the black dots in Fig: 4.1. They are one HWHM away from

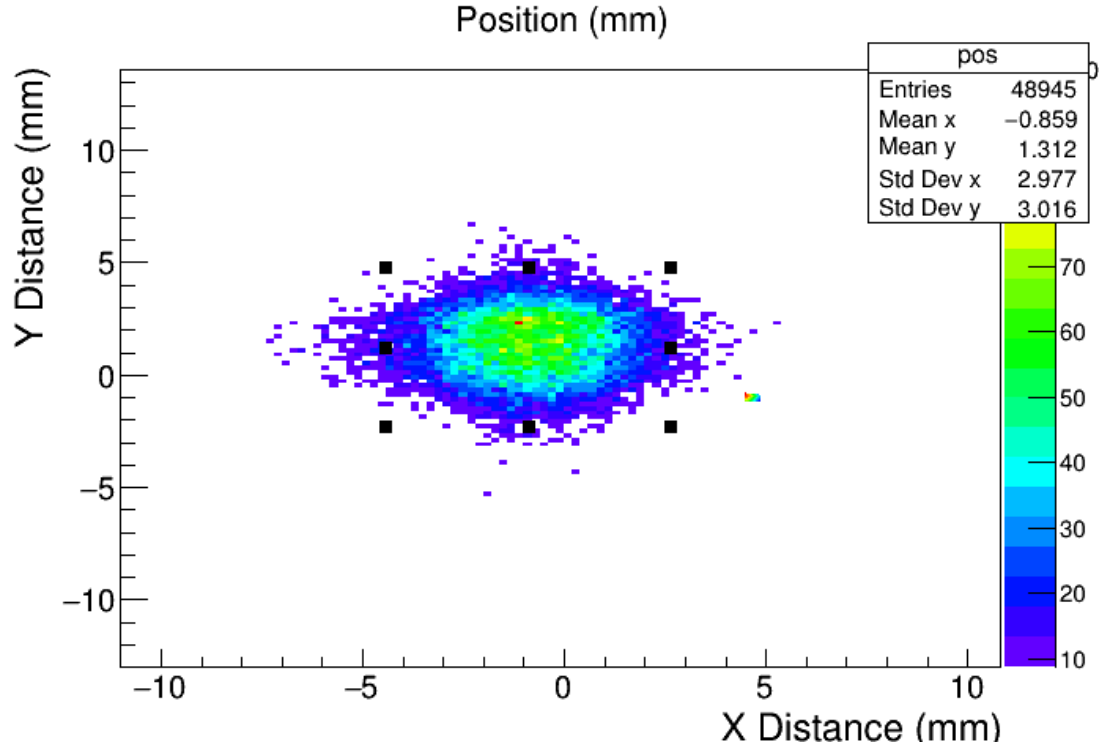


Figure 4.1: The beam spot of the calibrated PPAC spectrum. The samples of the spectrum that were averaged together are shown in the black dots. The center of the fit is not shown.

the center.

After averaging the 8 points, the range on the z axis was taken from the average of those points to the top. The resulting beam was measured to be 8 mm by 6 mm large.

This is the size of the spot at the PPAC. Ion optics simulations were used to build the cross section of the beam at the PPAC and at the target. Using these cross sections, the magnification between the two locations was calculated. The magnification was different between the x and y directions.

### 4.2.2 Beam Purity

The beam was filtered by S800 spectrograph. The purity measured there was at 93%, with the main contaminates being  $^{18}\text{O}$  and  $^{19}\text{O}$ . This was measured up stream of the detector

set up. To double check the beam purity, two detectors were used. One was a thin Si PIN detector that was used as a sectionE detector. The other detector was a small CsI(Na) detector similar to the implant detector that was used during the steering and during the beam size measurement. It had a much lower voltage than the one used for the implantation measurement. Both of these in tandem were used to build a particle identification plot. From this, it was found that the beam is very clean.

## 4.3 Detector Set Up

### 4.3.1 $^{20}\text{F}$ Decay Detectors

One scintillator was a 3 in diameter by 3 in long cylinder of EJ-200 polyvinyltoluene (PVT). It was attached to a clear plastic disk attached to a photomultiplier tube. The idea was to avoid a rate dependent gain effect that was seen in a previous experiment. The plastic detector signal is fast (around 100 ns) which makes pile-up a lesser concern. This detector was built by collaborators for this experiment. During the experiment the voltage on the PMT of this scintillator was varied. This was due to an observed distortion in the beta decay spectrum. A gain monitoring system was installed.

To monitor the gain of the plastic detector, a plastic disk containing an optical fiber was placed between the crystal and the photomultiplier tube. The other end of the fiber was fed into a box with an LED driven by a function generator. The box was made light-tight with electrical tape and black paint. An additional optical fiber fed the light to a Si PIN diode. This was to monitor the light output of the LED.

To help check for systematics effects, another implant detector was used. It was a 2 in by 2 in by 4 in CsI(Na) detector. This detector was a module from the CAESAR array [17].

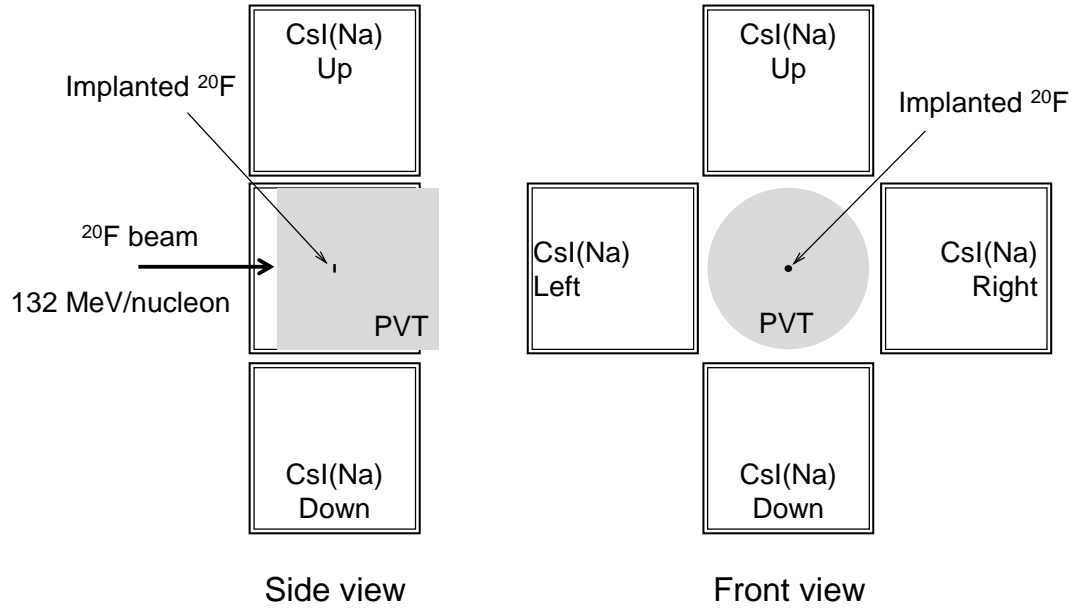


Figure 4.2: A sketch of the detector set up. Shown here is with the PVT detector implant. The CsI (Na) detector was centered in the middle of the the four gamma detectors and recessed by 1 inch. The bottom image shows a side of the detector set-up.

It does not have any gain monitoring like the PVT detector, but it is similar to a detector used in a different experiment. The other experiment was a similar measurement with  $^6\text{He}$  instead of  $^{20}\text{F}$ .

In order to measure the gamma ray from the  $^{20}\text{F}$  decay, a frame was built to hold four cubic 3 in CsI(Na) detectors. These were also part of the CAESAR array. The frame to hold the four detectors was designed to be able to move the four outer detectors around in various configurations. However, no other configurations were used during the experiment.

A sketch of both detector configurations is shown in Figure 4.2.

To switch between different implant detectors, the central detector in the frame was removed and put on the floor. The other detector was placed in the center of the four gamma detectors. The PVT detector was supported on a metal rail, while the CsI (Na) detector was supported on pile of scrap aluminum.

### 4.3.2 Other detectors

The light from the LED was also piped to a PIN diode. This was to get an independent measure of the light from the LEDs. A parallel plate avalanche counter (PPAC) was used for beams size measurements. A Si detector was used to check the beam purity. A pulser was used to make sure the data acquisition clock was stable.

### 4.3.3 Powering the Detectors

To power the gamma and implant scintillators, 3 2-channel NHQ 212M ISEG power supplies were used. The Si detector was powered by a Tennelec TC248 amplifier. The PPAC was powered by an integrated power supply.

Each detector had a different voltage. The PVT implant detector was varied in voltage over the course of the experiment. This was due to concerns about saturation effects. Initially, the high voltage on the PVT detector was chosen to take advantage of the dynamic range of the detector. For the PPAC, The voltage for the four gamma detectors was chosen so that they had roughly the same gain. The voltages of the detectors is shown in table ??.

| Detector               | HV (V) |
|------------------------|--------|
| PVT Implant (Sets 1-4) | -975   |
| PVT Implant (Set 5)    | -856   |
| PVT Implant (Set 6)    | -780   |
| CsI (Na) Implant       | 780    |
| CsI (Na) Gamma 1       | 930    |
| CsI (Na) Gamma 2       | 1000   |
| CsI (Na) Gamma 3       | 970    |
| CsI (Na) Gamma 4       | 1015   |
| Si Pin                 | 20     |
| Pin diode              | 15     |
| PPAC                   | 560    |

During the implantation cycle, a large amount of current was generated in the implant

detectors. In order to counteract this, a limiter box was installed for the PVT detector for sets 3 to 6. The limiter box had several relays that cut the power to the PVT detector's photomultiplier tube during the beam on cycle. To accomplish this, the limiter box was given the same signal that fed the beam on/beam off for the cyclotrons. For the CsI(Na) implant detector, the HV supply had the current limiter enabled. This accomplished the same thing.

For the depth of the implantation of the beam, ion simulations were used. The LISE++ program was fed the beam meagnets. It was given the energy of the beam and the detector set up. It then calculated the depth of the implantation of the detector and the range of the depth inside the detector. This gave a depth of 3.02 cm in side the PVT detector and a depth of 1.156 cm in the CsI(Na) detector. The range of the depth was 1.2 mm in the PVT detector and 0.4 mm in the CsI(Na) detector.

#### **4.3.4 Verification of Implant Depth**

In order to verify the simulations for the beam implant depth, a degrader was inserted into the beam for a beam depth measurement. The degrader was made of aluminum and had two different thicknesses: 7.89 mm and 11.38 mm. The beam was caught by a CsI(Na) scintillator of a similar design to the one used for the implantation measurement. The angle of the degrader was changed to change the ective thickness of aluminum that the beam had to travel through. By varying this thickness to the one predicted to stop the beam out side of the detector, the depth of implantion could be verified. This was done after the main run, and the simulations proved to be correct.



## 4.4 Experimental Conditions

The data was taken in runs of roughly one hour. However, many runs were cut short when the DAQ stopped recording data for one of the detectors. In order to properly measure the decay, the beam was pulsed with an implantation time of anywhere from 1 to 2 seconds, and a decay time ranging from 22 s to 32 s. The beam was turned off since the light from the implantation of the beam would drown out any signal obtained. A run with a decay time of 60 seconds was also taken for each implant detector.

To achieve the beam pulsing, two timer boxes were used. A CAEN N1145 quad scaler module was used to control the beam off time. This module had a digital control of time down to 1 ms. Once the time finished counting down, a signal was sent to a second module. A CAEN N93B dual timer used the signal from the quad scaler as a start signal. The time period was set using a dial, which was less precise. Once the dual timer finished its time, it sent a signal back to the quad scaler to restart the cycle. The output of these two modules created a signal with one voltage level during the dual timer's time and another voltage condition during the quad scaler's time. This signal was fed into a box. The voltage level during the quad scaler's time dephased the cyclotron RF, turning the beam off. When the dual timer voltage level occurred, the RF returned to the tuned value, turning the beam on.

# Chapter 5

## Data Processing

The detector were tested using an oscilloscope to check for their signals. The signals were then inserted into a digital data acquisition system.

### 5.1 Data acquisition

All the signals for all the detectors were sent to digitizers. These digitizers were three 250 mega-samples per second 16 channel XIA PIXIE modules. They were run with the digital NSCL system. The first module had the implant detectors and the four gamma detectors. The second module had five signals from the PPAC and one signal for the Si dector. Both of these had the beam on signal, beam off signal, a 100 Hz pulser, and the signal from the PIN photodiode. The third module only recorded the digitized waveforms from the PVT detector.

Each of the channels on each of those modules outputted a time stamp and an energy calculated from a trapezoidal fitler. The third module output the digitized waveform over 400ns. The digitizers took samples every 8 ns. The clock used was a stable EPSON SGR-8002JC programmable crystal oscillator.

The first thing the PIXIE modules did was to digitize the wave forms of the signals. The digital wave forms of the signals were only saved for the PVT implant detector. The PIXIE modules' software applied a trapezoidal energy filter to the digital wave froms.

### 5.1.1 Filter Description

The parameters of the trapezoidal filter needed to be set by hand. First, three sums of the digitize wave-forms were taken. The first sum was over a time known as  $tPEAKING$ . Then, a second sum was taken directly after the first over a time known as  $tGAP$ . Then, a third sum was taken directly after the the second with over a period of  $tPEAKING$  again. These three sums were added with equation ??

$$E = C_0 * S_0 + C_g * S_g + C_1 * S_1 \quad (5.1)$$

with  $S_0$  being the first sum over tPeaking described above,  $S_G$  being teh sum over tGap, and  $S_1$  being the second sum over tPeaking.  $C_0$  is described in equation ??

$$C_0 = \frac{-(1 - e^{\frac{tSPL}{\tau}})e^{\frac{tPEAKING}{\tau}}}{1 - e^{\frac{tPEAKING}{\tau}}} \quad (5.2)$$

where  $tPEAKING$  is the time described above,  $tSPL$  is the 8 ns sampling time, and  $\tau$  an additional tunable parameter.

$C_g$  is described in ??

$$C_g = 1 - e^{\frac{tSPL}{\tau}} \quad (5.3)$$

with the same variables. Finally,  $C_1$  is described in ??.

$$C_1 = \frac{1 - e^{\frac{tSPL}{\tau}}}{1 - e^{\frac{tPEAKING}{\tau}}} \quad (5.4)$$

With the same variables. This filter averaged the background before a pulse in  $C_0$  over  $tPEAKING$ . It took a sample of the pulse, averaged over  $tPEAKING$  again in  $C_1$ . Then,

it subtracted off  $C_0$  from  $C_1$ , after adjusting for the exponential decay of the pulse. The time constant of that decay is the  $\tau$  parameter. When tuning the PIXIE system, the  $\tau$  parameter has the most effect on the output energy.

For this experiment, the various filter parameters are summarized in table ??

Table 5.1: Energy Filter Parameters

| Detector               | $\tau$    | $tPEAKING$ | $tGAP$ |
|------------------------|-----------|------------|--------|
| PVT implant            | 60 ns     | 208 ns     | 128 ns |
| All CsI (Na) Detectors | 900 ns    | 480 ns     | 48 ns  |
| PPAC Channels          | 300000 ns | 1200 ns    | 96 ns  |

There was also a trigger filter in the PIXIE system. The filter was the same, but the times were much shorter, so that the trigger filter could work quicker. There was a threshold that the output of the trigger filter had to be above in order to be recorded. The times for the trigger filter were half that of the energy filter.

### 5.1.2 Data Acquisition Software

In order to set the parameters of the various filters, a program called NSCOPE was used [?] The program GUI was used to set the rise time, the gap, and the threshold for both the energy filter and the trigger filter. These parameters were set differently for each detector type. The CsI(Na) detectors (the implant and the 4 gamma detectors) shared the rise time and gap time, while other detectors had different parameters. Sample spectra were taken with NSCOPE, and the parameters saved to a file.

This file was loaded with a program called ReadOut, which ran the data taking. The ReadOut program used a ringbuffer in order to record the output of the data. The program recorded data as an .evt binary file if the record data button was checked.

The ringbuffer was also fed to a program called scalers. This gave the rates of the events coming into each channel. It gave an input rate to each channel, the recorded rate, and the total over each run. This was to check how each channel in each module was doing.

For online analysis, a program called SpecTcl was used. It took the evt files and processed them into histograms. These histograms could be put in coincidence. Displays of the implant detector energy and rate were displayed. The energy of the implant vs time was also displayed. Additionally, the implant energy vs time since last beam on was plotted as a 2-D spectra. The decay curves (time in implant minus last beam on) were also plotted. These histograms were used as diagnostics.

## 5.2 Data Taking and Processing

To take data, the ReadOutGUI program was activated. Data was taken in one hour intervals, unless one of the detectors stopped counting early. If a detector stopped early, it was the up detector. The run was then ended early and then a new one restarted. The events built by Readout had a time interval of 1000 ns.

The resulting .evt files of ReadOut were processed using a program called DDAS dumper. This converted the .evt files to ROOT files. These ROOT files contained a TTree that had the energy and time stamps of each detector. There was also information on the trace of the detector.

From the ROOT files from the ddasdumper, another ROOT file was built. These files were processed with a modified version of a program called *scan*. The original version was written by Stan Paulauskas. First, the various energies and times for each detector were built into a histogram. Then, the energy and times for the implant detectors, four gamma

detectors, beam on signal, and beam off signals were saved to a variable. This information was used to build new events for a new TTree.

Each event started with a non-zero energy reading in any of the five detectors. Then, a 400 ns long time gate opened, during which all energies and times were saved into the event. The time signatures of the last beam on and beam off signals were also saved into each event. The energies of the beam on or beam off signals were 0 or 1.

# Chapter 6

## Half Life Measurement

### 6.1 Motivation

During the experiment, it was noticed that there was a disagreement between different values of the half-life. As a side project and as a chance to thoroughly investigate the data, a half-life measurement was taken. The previous measurements of the half-life of  $^{20}\text{F}$  are shown in Figure 6.1.

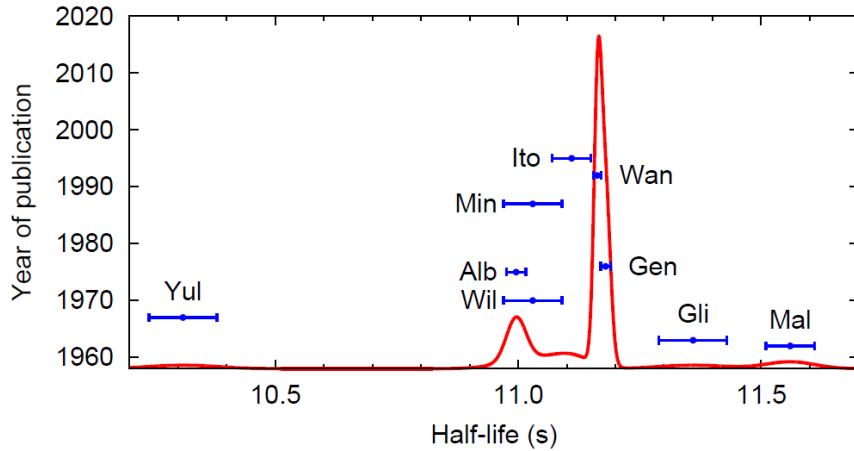


Figure 6.1: Previous measurements of the  $^{20}\text{F}$  half-life. The labels correspond to: Mal [10], Gli [7], Yul [21], Wil [18], Alb [1], Gen [6], Min [11], Wan [16] and Ito [8].

This ideogram has a red line which is a sum of Gaussian functions. The centroids of the Gaussians are the central values of the measurements. The sigmas are the errors, and each gaussian is weighted by  $\frac{1}{\sigma^2}$ . This is to see that there are two different values that the half-lives are converging to.

It has been used in the past for searches of second-class currents and in astrophysics.

## 6.2 Half life data analysis

First, the data was processed as described in the previous chapter.

### 6.2.1 Data Selection

Only the data from the PVT impantation set was used for the half-life analysis. Afterglow was present in the CsI(Na) detector. This caused a slow pile-up effect, where a higher rate means more light. The extra light pushed events at higher rates towards higher energies. For the decay curve, it meant that at earlier times, the effective gain of the implant detector was higher. The beta cuts, however, stayed in the same position. Early in the decay cycle, events near the cuts could start out inside the window. As time went on and the gain changes, these cuts could move below the lower beta cut. Due to the shape of the beta spectrum, the higher the lower beta cut, the larger the effect. This effect is seen in Figure 6.2.

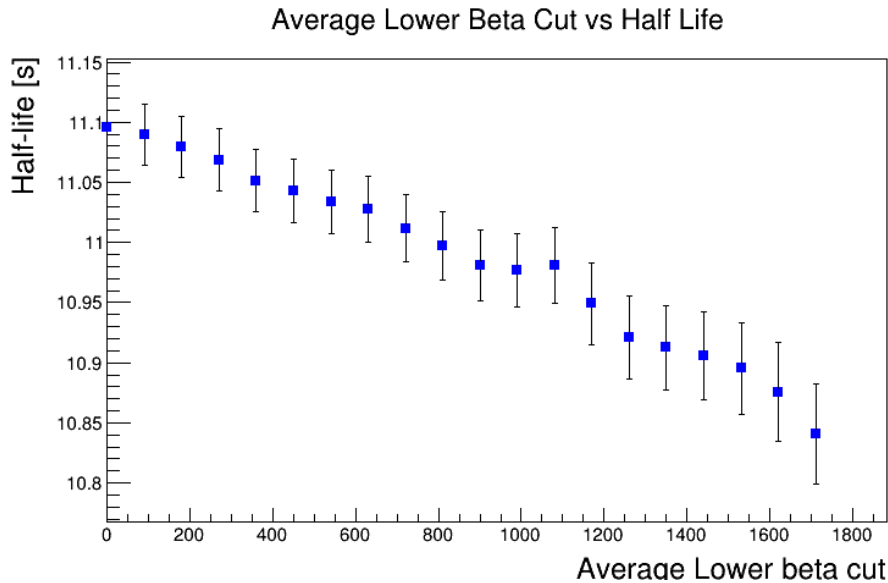


Figure 6.2: The effect of the lower beta cut vs the half-life in the CsI(Na) data



Attempts were made to counteract this effect with a more sophisticated analysis. The beta spectrum was built and fitted second by second in order to obtain a time-dependent calibration. The gain of the calibration was plotted as a function of time and fit with a line. The offset of the calibration was seen to be independent of time. The resulting time-dependent calibration was used to analyze the data. This reduced the effect seen in Figure 6.2, but did not entirely eliminate it. Since the CsI(Na) data has a small statistical impact, it was decided to eliminate that data from the analysis of the half-life.

The plastic scintillator did not have any afterglow, so the PVT implant detector was immune to this effect. The PVT data was separated into 7 sets. A summary of the set conditions is shown in Table 6.1 As shown in the table, the major conditions were the PVT high voltage, the inhibitor box, and the beam current.

Table 6.1: The PVT runs

| Set | Beam on Time [s] | Measuring Time [s] | PVT HV [v] | HV Inhibit Installed | Beam intensity [nA] | Runs |
|-----|------------------|--------------------|------------|----------------------|---------------------|------|
| 1   | 1.67             | 30                 | -975       | No                   | 30                  | 9    |
| 2   | 1.67             | 30                 | -975       | No                   | 93                  | 2    |
| 3   | 1.67             | 30                 | -975       | Yes                  | 30                  | 9    |
| 4   | 1.67             | 30                 | -975       | Yes                  | 93                  | 11   |
| 5   | 1.67             | 30                 | -856       | Yes                  | 30                  | 93   |
| 6   | 1.00             | 60                 | -800       | Yes                  | 93                  | 1    |
| 7   | 1.10             | 20                 | -780       | Yes                  | 93                  | 10   |

The inhibitor box was not installed until the third set of data. The inhibitor box shut off the high-voltage during the beam on period. Without the box, the current on the PMT was saturated during the beam on period. This caused a gain shift over time as the power supply recovered. This time-dependent gain shift caused large systematic errors when the beta cuts were moved. Thus, sets 1 and 2 were not used in the final analysis, but are listed here for completeness's sake. These gain shifts can be seen in Figure 6.3.

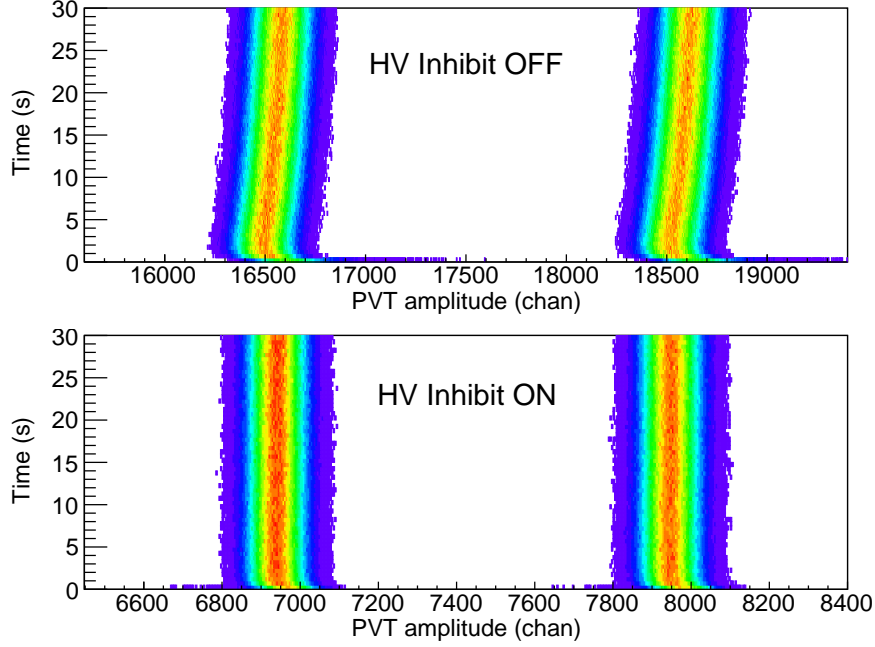


Figure 6.3: The light pulse as a function of time for set 1. The gain changes smoothly over time. This causes a large change in the half-life as the beta cuts are moved.

## 6.2.2 Cut Selection

In order to do the half-life analysis, software coincidences were imposed. Three conditions were set in total. Two conditions were on the energy in the implantation detector and one of the four CsI(Na) detectors. An additional condition on the time difference between the events recorded in the two detectors. A sample spectrum of all the gamma and beta energies is shown in Figure 6.4

Fixed energy gates were used for to select in the beta window for the PVT run sets. Each different data set had a different energy window due to the gain shifts. A sample spectrum with the gates can be seen in Figure 6.5. This spectrum was put in coincidence with the gamma spectra. The lower beta cut was selected to cut out the 511 beta spectram as seen in Figure 6.4. When gated around that energies, the resulting gammas measured by the large CsI(Na) detectors are consistent with  $^{10}\text{C}$  and  $^{11}\text{C}$ . This comes from the break-up of the

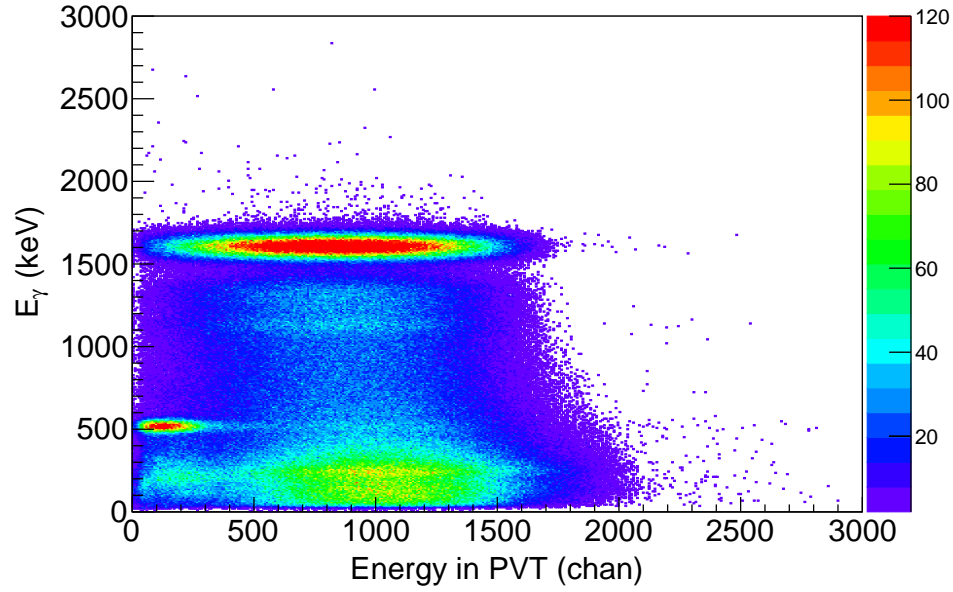


Figure 6.4: The 511 region can be seen in this graph

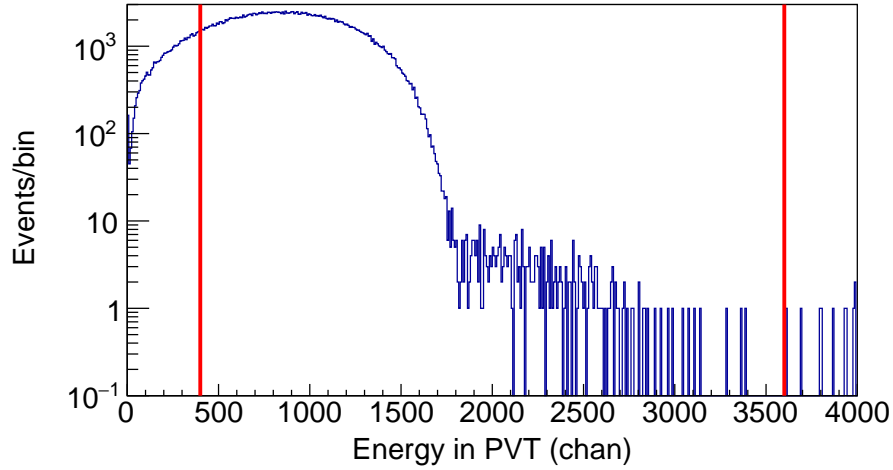


Figure 6.5: The lower beta cut was selected to be above the 511 region. The upper beta cut was selected to include all the pile up

plastic.

As described above, only the runs after the installation of the limiter box were used for the half-life analysis.

A time difference condition was set by building a spectrum of the time differences between

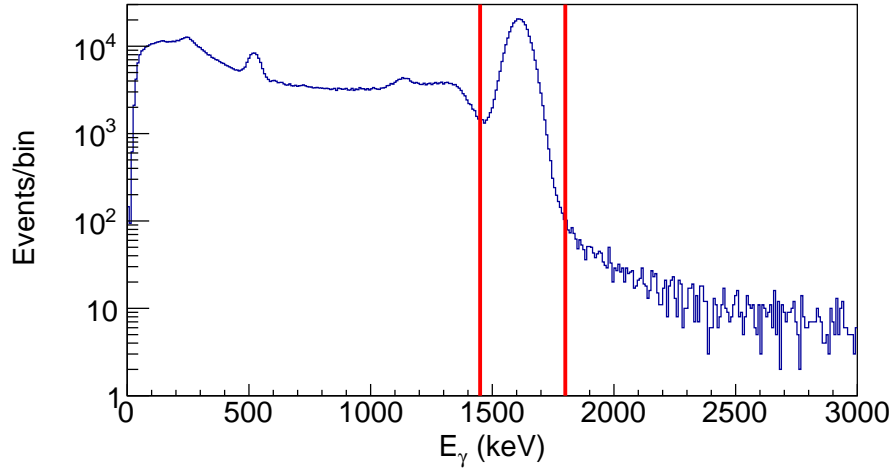


Figure 6.6: The wide cuts are to reduce the effect of the rate dependent gain.

the implant detector's event and one of the four gamma detector's events. The peak of this time difference spectrum was found, and an interval of  $\pm 24$  ns was used for this gate. A sample time difference spectrum can be seen in Figure 6.7

The time difference spectrum shows several features. First is the prompt peak, which are correlated gamma and beta events. To the right of the prompt peak, there is a pedestal of events. These come from pile-up events. What happens is that a  $^{20}\text{F}$  event decays and the time stamp of the emitted beta is recorded. The corresponding gamma ray is not detected. Then, within the pile-up window, a second  $^{20}\text{F}$  decays. The implant detector is dead and does not record the second time stamp. Due to pile-up, the time stamp of the second beta event is not recorded. The gamma ray is then detected at a later time compared to the first event. A cartoon sketch of this effect is shown in Figure 6.8. The pedestal can be seen in full in Figure 6.9.

The other events to the left of the prompt peak and to the right of the pile-up pedestal are accidental coincidences. These include the background coincidences.

The time signals for the outer four gamma detectors were used for the half-life analysis.

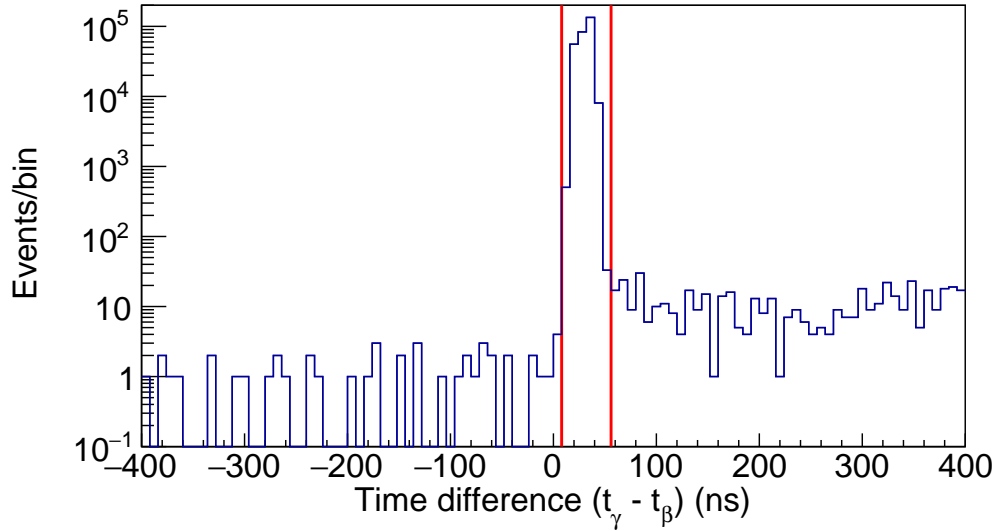


Figure 6.7: This is a gamma and beta energy filtered spectrum of the time difference between the up detector and the PVT implant detector. The tail on the right side of the large peak is due to pile up. The narrow time cuts are shown with a dotted line. The wide time cuts are shown with a solid line.

This gave 4 independent measurements of the half-life per run. Only full decay cycles were used. This was done by finding the last beam on and putting a condition on the run time of the events. The decays where the up detector stopped counting were ignored, as there were few enough that they did not make a difference.

The dead time was corrected using measured rates and a dead time of 464 ns for the implant detector and 656 ns for the gamma detectors. The dead time was measured by building a spectrum of the time difference between consecutive time stamps. The lowest time difference was taken as the dead time. This was checked using the light pulser in the PVT detector. For each gamma detector, a histogram of the energy-filtered rate was built. The unfiltered implantation detector rate and gamma rate was built. Using the uncorrected rates as an input, the gamma detector rate was corrected for bin by bin. The correction

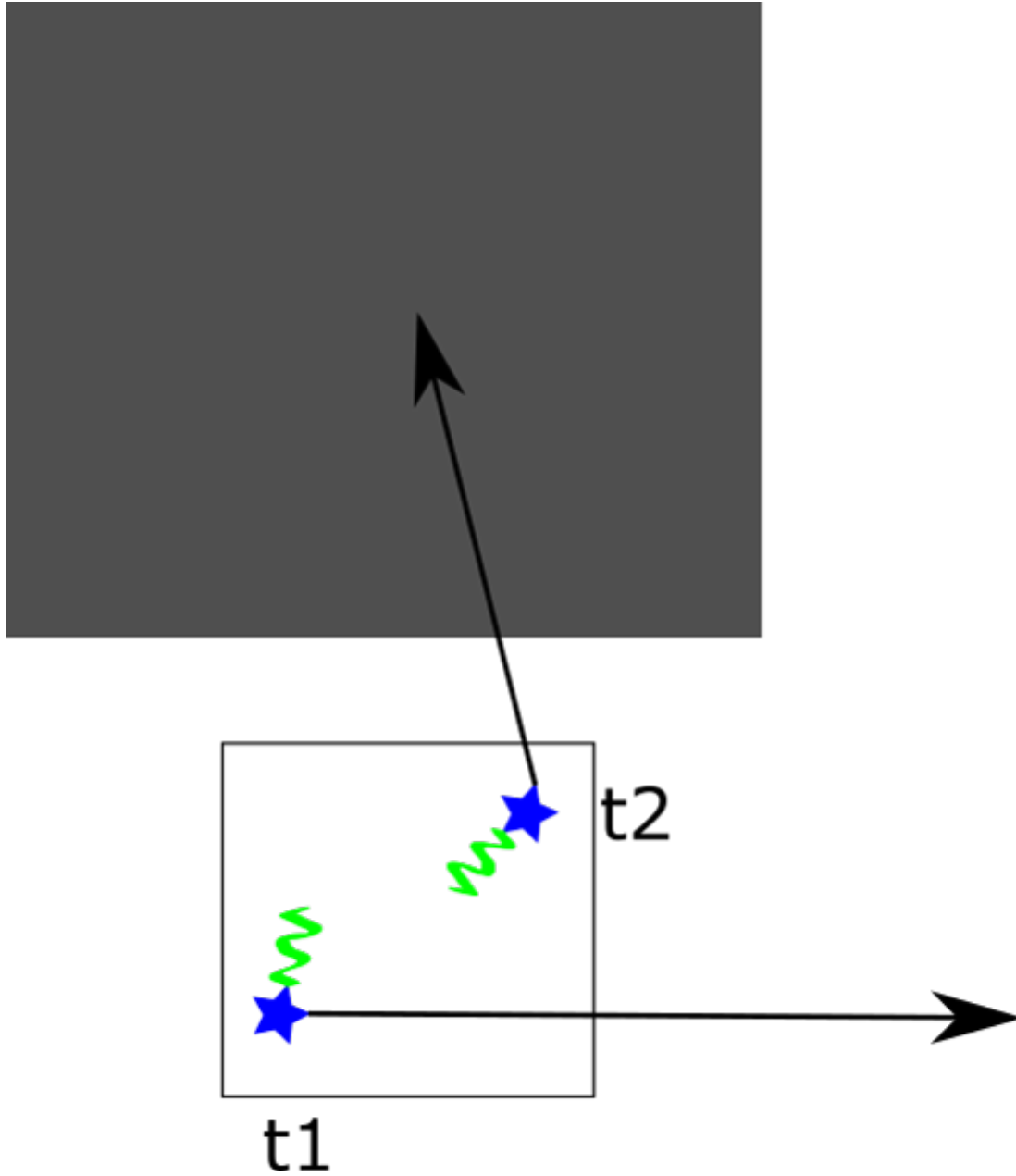


Figure 6.8: A sketch of the pile up events. A  $^{20}\text{F}$  decay happens at time =  $t1$ . The green electron is detected in the implant detector. The black arrow (the gamma ray) is not. Then, later at time =  $t2$ , another  $^{20}\text{F}$  decays.  $t2$  is within the pile-up window of  $t1$ . Both electrons energies pile-up and are added together. However, the time stamp recorded by the DAQ is still  $t1$ . The gamma ray from event  $t2$  can be detected in a gamma detector at time  $t2$ . This creates the uncorrelated event pedestal in the time difference graph.

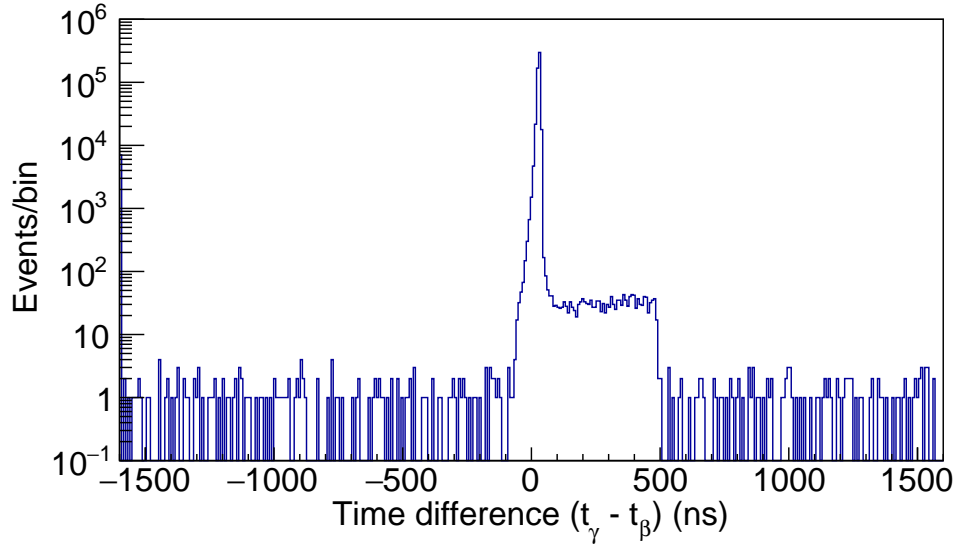


Figure 6.9: The time difference spectrum zoomed out. This figure is shown with energy coincidences.

used is shown in equation 6.1

$$r_{coincidence}^c = \frac{1}{1 - r_\beta \tau_\beta} \frac{1}{1 - r_\gamma \tau_\gamma} r_{coincidence}^m \quad (6.1)$$

where  $r_{coincidence}^c$  is the corrected gamma-beta coincidence rate,  $r_\beta$  the raw measured implant rate,  $\tau_\beta$  the dead time of the implant detector,  $r_\gamma$  and  $\tau_\gamma$  the raw measured rate and dead time for the CsI(Na) detector, and  $r_{coincidence}^m$  the measured coincidence rate. Then, after corrected for the dead time, each cycle was added together relative to the last beam off. These stacked cycles were used to find the half life.

For high beam intensity runs (i.e. sets 4,5 and 7), the dead-time corrections had a size of 31 to 36 ms. For low beam intensity runs, (i.e. set 3) the dead-time correction changed the half-life by 6 to 8 ms. The values shown in this chapter are those with the dead-time correction.

Once the decay spectra were put in coincidence and stacked up, it was fit with equation

$$f(t) = a \exp(-t * \ln 2 / T_{\frac{1}{2}}) \quad (6.2)$$

where  $a$  and  $T_{\frac{1}{2}}$  are free parameters.  $a$  is the initial rate and  $T_{\frac{1}{2}}$  the half-life. The decay curves were fit from 1.5 seconds past the beam on time to 1.5 second from the end of the decay time. The fitting method used was the log likelihood method. The 60 second decay run up detector result is shown in Figure 6.10. From this run, it is seen that the spectra does not decay back down to the background. The lack of background parameter in equation 6.2 comes from this observation.

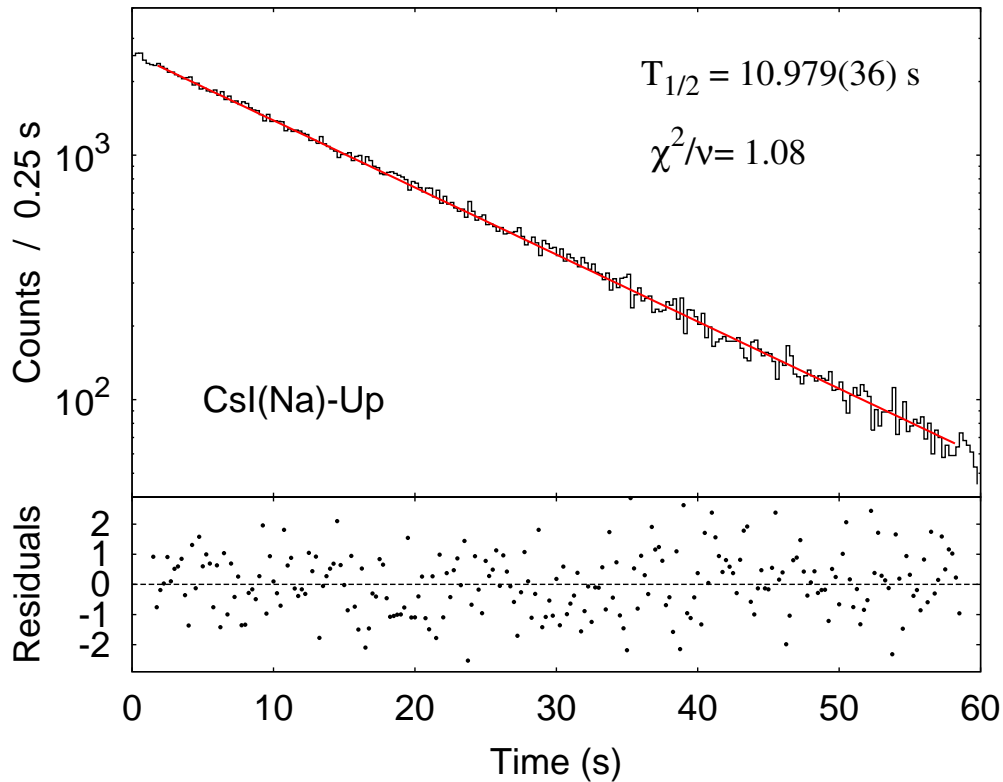


Figure 6.10: The decay spectrum from the up gamma detector is shown on the top graph. The red line is the exponential fit. The bottom graph shows the residuals from the fit.



The decay spectra were built run by run, and the resulting fitting results were averaged together. Runs with a p-value less than 0.05 were considered statistically insignificant and thrown out. After all the significant half-lives were collected, the average of them all was taken.

## **6.3 Systematic Effects**

Several systematic effects were looked at. The dead time correction was applied before any other systematics were investigated.

### **6.3.1 Dead Time**

The timing resolution of the clock is 8 ns. Due to this, there is an uncertainty on the dead times of at least 8 ns. The dead times were varied  $\pm 4$  ns and the half lives calculated. Half the difference of those half lives is the systematic uncertainty.

### **6.3.2 Pile Up Effects**

The dead time is overcorrected. Due to pile up, some of the pile up events are not totally lost. Some of the events thought to be missing just got shuffled around. This is a problem due to the fact that energy gates are imposed. The pile-up events also have a different time structure than the regular events. Due to the fact that the pile-up goes as the singles rate squared, the half-life of the pile-up events is half that of the non-piled-up events. This creates a background with a different time signature, and causes a change in half-life.

The 48 ns time cut around the peak, shown in Figure 6.7, was compared to several other, larger time cuts. The narrow time cut still have some uncorrelated background and pile-up

events in them.

To account for this effect, several other time cuts were taken. These cuts were plotted vs half-life. This graph was fit with a quadratic function. This function was extrapolated to zero, which was the correction due to the pile-up. This graph is shown in Figure 6.11.

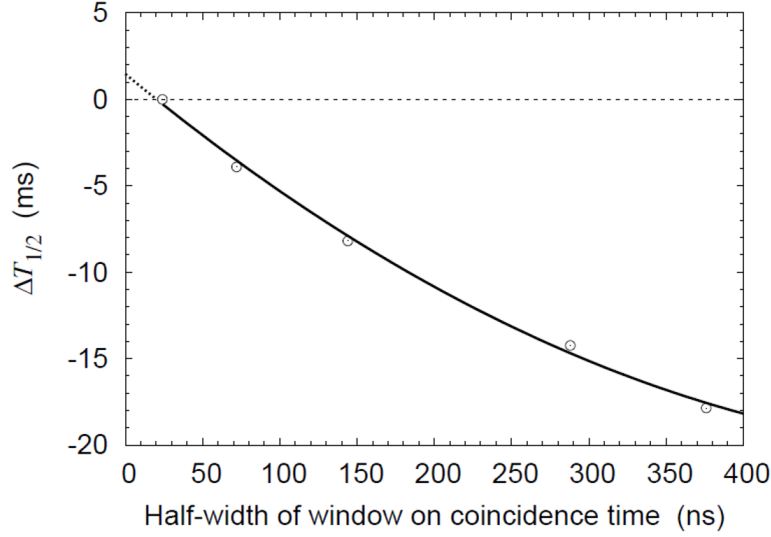


Figure 6.11: Time difference vs the resulting half-life. The line is a quadratic fit which was extrapolated to zero.

The extrapolation line is shown. The half-life was corrected to the zero value of the window. The difference between this extrapolated value and the previously measured value was taken as a correction and as an error bar.

### 6.3.3 Background

The first systematic effect is the effect of background. Due to the low decay time, directly fitting a background is impossible. There is no background region for the fitting function to anchor to, which induces a large correlation between the background and the half life. Several techniques were used to estimate the background.

### 6.3.3.1 Simultaneous vs Seperate Fitting

The first attempt was by simultaneously fitting each run with a different fitting function.

The equation used was equation 6.3.

$$f(t) = a(\exp -t * \ln 2 / T_{\frac{1}{2}} + b) \quad (6.3)$$

with  $a$  and  $T_{\frac{1}{2}}$  the same as in equation 6.2 and  $b$  the relative background level. The half-life of the four detectors was set to be a common parameter. The relative background level and initial rate, however, were assumed to be independent for each spectrum. The resulting half life was compared to the value found with fitting each detector seperately without a background.

The effect of adding a background was investigated using Monte Carlo. Exponentials were generated and an ammount of background added. The resulting function was fit with a decay curve without a background parameter. The amount of background added was varried, and the resulting half lives plotted. It was found that increasing the background decreased the value of the half life, and that the background level and the half life value were strongly correlated.

A similar Monte Carlo was written to check the simultaneous fit method. Four decay curves were fitting and simultaneously fitted the same way was the data. They were also fitted seperately with only an exponential decay. The background was varied and the difference between the two values was taken. The method shows a trend similar to the one seen in the previous Monte Carlo.

In the data, it was discovered that the results of the simultaneous vs seperate fitting depended on the size of the dead time correction. If the dead time was overcorrected, it

induced an effect that was similar to having a larger background. If more dead time was imposed, the effect was as if there was a negative background. A dead time correction was added to the Monte Carlo, and a similar trend was seen. As long as the dead time is known exactly, the background can be extracted with this technique. However, as it is somewhat uncertain of what the exact dead time should be, this technique cannot be used to determine the background.

### 6.3.3.2 Spectra Arguments

The other way to try and gauge the background size is to look at the spectra. Looking at Figure 6.7, it can be seen that on the left side of the large peak, there are very few counts. It can also be seen that the prompt peak in the center contains most of the counts, while there is a long tail on the right side of the peak. This tail is due to pile up. An event in the beta window piles up with another event later in time. The second event is read by a gamma detector, but is correlated with the first event, causing the large time difference. The time spectrum changes if the beta spectrum is cut in different ways.

In the gamma beta spectrum, it can be seen that there is no background events aside from the 511 region. This is due to the presence of  $^{10}\text{C}$  and  $^{11}\text{C}$ . When the detectors are put into tripple and quadruple coincidence, the gamma rays of those isotopes appear. There are no gamma rays in the 1620 keV window which was filtered on.. The only coincidence possible is if there is pile up into that window along with a beta event. The estimate of those events is shown on the left side of the peak in the time difference figure shown in Fig. 6.7 These events are accounted for when extrapolating the different time difference cuts, as shown in Figure ??

### 6.3.4 Cut Sensitivity

For each pair of detectors, there were four conditions: two for each the implant and gamma detectors. For the gamma cuts, the edges of the gates were varied  $\pm 5$  keV in each direction for each cut. The results is insensitive to the upper beta cut. The lower beta cut was scanned with 6 different values going evenly from the initial lower beta cut to the peak of the spectrum. Moving the lower beta cut also effects the dead time correction. In order to disentangle the two, the lower beta cut was varied with two different time difference conditions. The location where the difference between the two calculations blows up is where the effect of the lower beta cut starts being swamped by the effect of the pile up. This is limit of where the lower beta cut was scanned. All four of these conditions were varied independently, and the procedure of generation the spectrum and fitting the decay curves was done. Half the resulting range of half-life values was taken to be a systematic uncertainty.

The fitting range of the decay spectra was varied. The start of the fit was varied bin by bin up to 6.5 seconds into the decay spectrum. The end of the fit was varied the other way to cut out the end of the decay spectrum. Since there was no noticable systematic effect, there was no increase in error associated with this effect.

### 6.3.5 Oscillator Stability

The oscillator of the PIXE board has a stability of  $\pm 5 * 10^{-5}$ . All times in the analysis were stretched by this value, and the half life calculated. Have the difference between the stretched value and the original value is another systematic error.

### 6.3.6 Binning and Fitting

In order to check the sensitivity of the result to binning, the decay curves were rebinned by a factor of two. Half the difference between the rebinned half life and the original half life is considered the correction and the uncertainty.

For the fitting method, log-likelihood estimators were used to fit the summed data. This was done with two different packages which gave identical results. This was compared to analytic results, which gave the same results, so the half life is insensitive to the fitting method.

## 6.4 Result and discussion

The PVT runs are shown in Figure 6.12

The results for the PVT runs are shown in in table 6.2 for the PVT runs.

Table 6.2: The PVT runs

| Detector | Half-Life | Error  |
|----------|-----------|--------|
| Up       | 11.0195   | 0.0088 |
| Left     | 10.9944   | 0.0087 |
| Down     | 10.9980   | 0.0085 |
| Right    | 10.9987   | 0.0095 |
| Mean     | 10.9999   | 0.0044 |

The size of the systematic errors investigated are shown in table 6.3

After the dead time correction, the value of the half-life from the CsI(Na) implant detector runs was found to be  $11.0011 \pm 0.0069$  (stat)  $\pm 0.0030$  (syst) s.

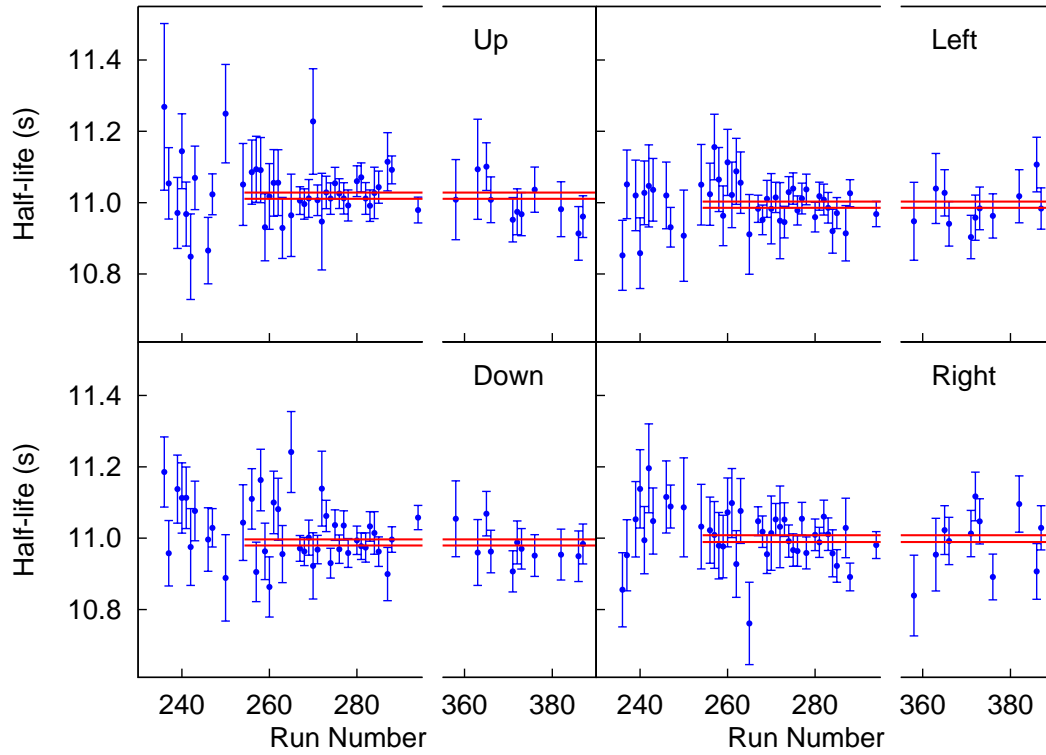


Figure 6.12: The red lines show the results of the fits over the runs that were used. The additional half-lives shown are excluded to reasons discussed previously.

Table 6.3: Systematics

| Source               | Correction [ms] | Uncertainty [ms] |
|----------------------|-----------------|------------------|
| Dead-time            | 0.00            | 0.24             |
| Oscillator stability | 0.00            | 0.80             |
| Lower PVT cut        | 0.00            | 2.32             |
| Lower gamma cut      | 0.00            | 0.15             |
| Upper gamma cut      | 0.00            | 0.05             |
| Uncorrelated events  | 1.47            | 1.47             |
| Binning              | -0.30           | 0.30             |
| Total systematic     | 1.17            | 2.89             |

## 6.5 Conclusion

The half-life measured is most consistent with some previous measurements of a half-life of about 11 s. This can be seen in Figure 6.13. This measure disagrees with the most recent

measurements.

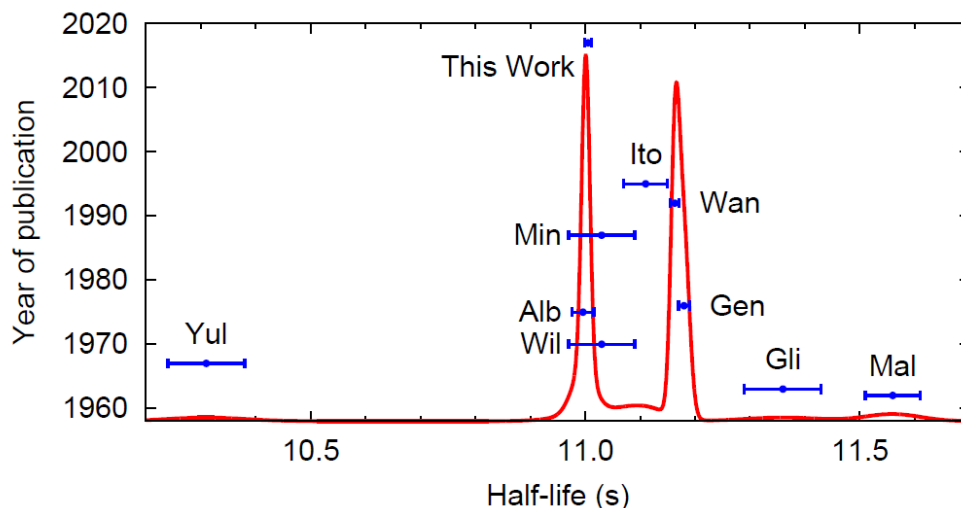


Figure 6.13: A scatter plot of (a) previous values with this work added. The labels correspond to: Mal [10], Gli [7], Yul [21], Wil [18], Alb [1], Gen [6], Min [11], Wan [16] and Ito [8].

Several things about the data set were discovered. It was learned that there were contaminants coming from the fragmentation of the  $^{12}\text{C}$  in the plastic scintillator. The beta decaying products could be a cause of why the beta spectrum for the PVT detector looks so odd. It was also discovered that the rate dependent gain effect in the CsI(Na) implant detector is significant. Before doing this measurement, it was assumed that the low rates would make that effect negligible. It was learned that after the coincidence, the amount of background left in the spectrum is negligible, and that we have no contaminants in the beam.



# Chapter 7

## Fitting Beta Spectrum

In order to get a measurement of the Fierz term, the spectrum shape needed to get fit. The effect of bremsstrahlung and the efficiency of the detectors needed to be accounted for. The way this was done was with a simulation.

### 7.1 GEANT4 Monte Carlo

The corrected beta decay spectrum was fed as input to a Monte Carlo. The program used to model the detectors was GEANT4. In order to use the program, parameters must be introduced.

#### 7.1.1 Detector Simulation

The geometry of the detector set-up was programmed into the simulation. The implant detector was modeled as a square prism of CsI. The rectangular prism was 9.76 cm deep with a 5 cm square base. The front edge implant detector was put at the center of the simulation. The aluminum sheath and MgO layer was not simulated for the implant detector.

The four large gamma detectors also square prisms. The active volume was 79.5 mm square and 76.2 mm deep. It was also made of CsI. Around this detector, a 1.5 mm layer of MgO was added. On top of this, the can of aluminum, 1 mm thick, was added into the

simulation.

The four large gamma detectors were arranged into a square around the implant detector. Each square base of the gamma detectors was centered one inch upstream from the face of the implant detector. This modeled how the implant detector was recessed in the experiment.

### **7.1.2 Source Definition**

The next step was to define a region inside the implant detector. This region was where the gamma and beta particles originated from. The depth of the region was calculated using LISE++, a ion optics code. The verticle and horizontal size of the region was calulated by using the PPAC measurement and an ion optics simulation. This size was 0.4 mm deep, 3.5 mm wide, and 3.6 mm tall. The source was implanted 1.156 cm into the detector.

Once these parameters were known, GEANT4 was told to generate two particles. First, the corrected beta energy spectrum was sampled and an electron of that energy was generated inside the implant region. The beta energy spectrum was generated using all the corrections described in chapter (COME BACK TO THIS). The location of the electron was recovered, and a photon with an energy of 1.6 MeV was generated as well. The initital direction of the two particles was as isometric. These particles where then propagated through the detector setup.. GEANT4 uses a physics list that has all the interactions a particle could take. The physics list used was standard option 4. This list is better at low energy electron physics.

### **7.1.3 Primary Particle Definitions**

There were three primary particles generated. Two were photons and one was an electron. All three particles had an isotropic angular distribution. The origin points of all the primary

particles was the same.

One photon was the 1.6336 MeV photon from the  $^{20}\text{F}$  decay. The energy of this photon was not changed.

The electron was generated according to phase space spectrum (equation 2.3) times all the corrections. For the radiative correction, the electron was generated with the formula that assumes all real photon energy is absorbed (equation ??). However, this is not exactly true. In this case, due to the geometry, photons are absorbed totally if they are below 100 keV in energy. In order to properly see the effect of the real photon emission, the second primary particle is used.

After the electron energy is generated, a formula describing the energy spectrum of the inner bremsstrahlung photons is generated. This spectrum is written out in equation 2.12. Further discussion of this formula is found in the theory chapter. A cutoff of 50 keV is imposed to the formula, as it has a singularity at zero photon energy. Then, the formula is numerical integrated from 50 keV to the electron energy. This is the total probability that an electron emits a KUB photon. This number is compared to a random number from 0 to 1. If the random number is below the integral, the inner bremsstrahlung energy spectrum is sampled. The algorithm used for this sampling is the van Neumann method [15]. The sampled energy is given to the third primary particle. The energy of the electron is reduced accordingly.

After all three particles have their energies defined, they are propagated through the detector set up.

### 7.1.4 Simulation Results Processing

The particles were tracked and the energy deposited in each detector summed up. The energy deposited in the implant detector was further separated into two parts: Energy from the electron and the inner bremsstrahlung photon. Energy from the 1.6336 MeV photon. After the energies of the particles reached a certain threshold, the simulation of one decay was finished. All the energies deposited into each of the detectors was summed up and saved as an event in a ROOT tree. Then, the process was repeated. A new location inside the region was generated and another decay generated.

In order to get to get the necessary statistics,  $2 * 10^9$  events had to be generated. After the events were done, the simulation data was processed further. Much like the experimental data, the simulated data had to be filtered. The energy absorbed in the implant detector was filtered by the energy absorbed in the outer four gamma detectors in the simulation.

The filtered data was separated into two parts: Absorbed energy in the implant detector only originating from the electron. Absorbed energy in the implant detector with some contribution from the gamma ray. These energies were built into two different histograms. These two histograms had the detector resolution applied to it.

The convolution function was

$$\sigma = A\sqrt{E} \tag{7.1}$$

where  $\sigma$  was the energy resolution,  $E$  the energy, and  $A$  a constant found through a calibration.

#### 7.1.4.1 Pile-up Modelling

After the convolution, the simulation data was sent through a simulation to model pile-up. The model used for the CsI(Na) signals was a linear rise and then an exponential decay. The linear part went from 0 to 1 over 100 ns. The exponential piece started at 100 ns at 1 and decayed with a  $\tau$  of 760 ns. This analytic equation was scaled up or down to whatever energy was sampled. It was then fed into a model of trapezoidal filter of PIXIE. The math was the same as described in the chapter on data acquisition.

This model was tuned on calibration data. A run was taken of  $^{137}\text{Cs}$  at 25000 counts per second. A 2000 counts per second  $^{137}\text{Cs}$  run was used as a background and subtracted off. Then, samples of the background-subtracted spectrum were taken up to the end of the 661 keV peak. Monte Carlo methods were used to model the time difference between two samples. If the two samples fell within the pile-up window, then the piled-up signal models were fed into the trapezoidal filter. The calculated pile-up energy was saved to a histogram. If the two samples did not fall within the pile-up window, then they were not fed into the filter model and just filled into the histogram. The parameters were adjusted until the generated pile-up matched the measured pile-up in the spectrum. The results of the tuning is seen in figure ??

## 7.2 Calibration

In order to properly fit the energy spectrum, a calibration of the CsI(Na) detector had to be done. Several different energy lines were used to find the calibration and the energy resolution function. The lines were the 1.173228 MeV and 1.332.492 MeV gammas from a  $^{60}\text{Co}$  source, the 0.661657 MeV gamma ray from a  $^{137}\text{Cs}$  source, and the 0.511 MeV and

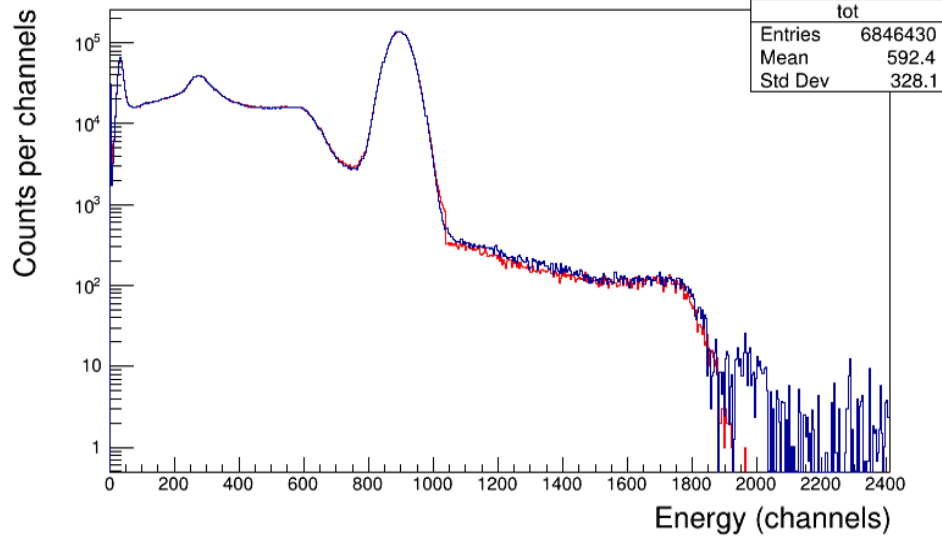


Figure 7.1: The tuning of the pile-up. The input spectrum is in blue. It was sampled up to 1000 channels. The generated spectrum is in red.

1.274527 MeV gamma rays from a  $^{22}\text{Na}$  source. These gamma rays were fitting with a gaussian and a background. The background varried from a linear background, a quadratic background, and an error function background. For the  $^{60}\text{Co}$ , both peaks were fit at once. These different background gave slightly different results for the centroids and the widths of the gaussians. The different widths and centroids were taken as a systematic error. From the centroids, the calibration for each detector was calculated as:

$$C = G * E + b \quad (7.2)$$

where  $C$  is the location of the peak in ADC channels,  $G$  the gain in channels/keV, and  $b$  the offset in channels. The widths of the peaks were calibrated with the gain and plotted vs energy. Then, equation 7.2 was fit to the results in order to determine  $A$ .

## 7.3 Fitting Procedure

The simulation described above were only part of what was needed. Other simulations included in the fit had the phase space times corrections times or divided an additional factor of the total energy of the electron. The simulations were all convoluted and filtered as described above. The various simulations were taken together and the fit using the ROOT algorithm.

I NEED TO EXPLAIN BETTER

## BIBLIOGRAPHY



## BIBLIOGRAPHY

- [1] D. E. Alburger and F. P. Calaprice. Half-lives of  $^{18}\text{Ne}$  and  $^{20}\text{F}$ . *Phys. Rev. C*, 12:1690–1691, Nov 1975.
- [2] I. Angeli and K. P. Marinova. Table of experimental nuclear ground state charge radii: An update. *Atomic Data and Nuclear Data Tables*, 99:69–95, January 2013.
- [3] William J. Byatt. Analytical representation of hartree potentials and electron scattering. *Phys. Rev.*, 104:1298–1300, Dec 1956.
- [4] Wolfgang Bhring. The screening correction to the fermi function of nuclear  $\beta$ -decay and its model dependence. *Nuclear Physics A*, 430(1):1 – 20, 1984.
- [5] S. A. Fayans. Radiative Corrections and Recoil Effects in the Reaction  $\bar{\nu}_e + P \rightarrow N + e^+$  at Low-energies. (In Russian). *Sov. J. Nucl. Phys.*, 42:590, 1985. [*Yad. Fiz.*42,929(1985)].
- [6] H. Genz, A. Richter, B.M. Schmitz, and H. Behrens. Half-life, endpoint energy,  $t$  value and shape factor in the  $\beta$  decay of  $^{20}\text{F}$ . *Nuclear Physics A*, 267:13 – 28, 1976.
- [7] S. S. Glickstein and R. G. Winter. Properties of  $f^{20}$ . *Phys. Rev.*, 129:1281–1283, Feb 1963.
- [8] S. Itoh, M. Yasuda, H. Yamamoto, T. Iida, A. Takahashi, and K. Kawade. Measurement of Beta-decay Half-lives of Short-lived Nuclei by Using High-rate Spectroscopy Amplifier. In *1994 Symposium on Nuclear Data*, Tokai, Japan, March 1995.
- [9] J.K. Knipp and G.E. Uhlenbeck. Emission of gamma radiation during the beta decay of nuclei. *Physica*, 3(6):425 – 439, 1936.
- [10] S Malmskog and J Konijn. Half-life measurements of  $^6\text{He}$ ,  $^{16}\text{N}$ ,  $^{19}\text{O}$ ,  $^{26}\text{F}$ ,  $^{28}\text{Al}$ ,  $^{77}\text{Se}$  and  $^{110}\text{Ag}$ . *Nuclear Physics*, 38:196 – 210, 1962.
- [11] Tadanori Minamisono. Nmr of short-lived nuclei implanted in crystals and a new isol for projectile fragments in relativistic heavy-ion reaction. *Hyperfine Interactions*, 35(1):979–991, Apr 1987.
- [12] B. Pfeiffer, K. Venkataramaniah, U. Czok, and C. Scheidenberger. Atomic mass compilation 2012. *Atomic Data and Nuclear Data Tables*, 100(2):403 – 535, 2014.
- [13] A. Sirlin. General properties of the electromagnetic corrections to the beta decay of a physical nucleon. *Phys. Rev.*, 164:1767–1775, Dec 1967.

- [14] D.R. Tilley, C.M. Cheves, J.H. Kelley, S. Raman, and H.R. Weller. Energy levels of light nuclei,  $a = 20$ . *Nuclear Physics A*, 636(3):249 – 364, 1998.
- [15] John von Neumann. Various techniques used in connection with random digits. pages 36–38, 1951.
- [16] T.F. Wang, R.N. Boyd, G.J. Mathews, M.L. Roberts, K.E. Sale, M.M. Farrell, M.S. Islam, and G.W. Kolnicki. Measurement of the half-life of  $^{20}\text{F}$ . *Nuclear Physics A*, 536(1):159 – 167, 1992.
- [17] D. Weisshaar, A. Gade, T. Glasmacher, G.F. Grinyer, D. Bazin, P. Adrich, T. Baugher, J.M. Cook, C.Aa. Diget, S. McDaniel, A. Ratkiewicz, K.P. Siwek, and K.A. Walsh. Caesara high-efficiency csi(na) scintillator array for in-beam ray spectroscopy with fast rare-isotope beams. *Nuclear Instruments and Methods in Physics Research Section A: Accelerators, Spectrometers, Detectors and Associated Equipment*, 624(3):615 – 623, 2010.
- [18] D. H. Wilkinson and D. E. Alburger. Mirror symmetry in the  $\beta$  decay of the  $a = 20$  and 25 systems. *Phys. Rev. Lett.*, 24:1134–1136, May 1970.
- [19] D.H. Wilkinson. Evaluation of beta-decay: I. the traditional phase space factors. *Nuclear Instruments and Methods in Physics Research Section A: Accelerators, Spectrometers, Detectors and Associated Equipment*, 275(2):378 – 386, 1989.
- [20] D.H. Wilkinson. Evaluation of beta-decay part v. the z-independent outer radiative corrections for allowed decay. *Nuclear Instruments and Methods in Physics Research Section A: Accelerators, Spectrometers, Detectors and Associated Equipment*, 365(2):497 – 507, 1995.
- [21] Herbert P. Yule. Half-lives of some short-lived radioactive isotopes. *Nuclear Physics A*, 94(2):442 – 448, 1967.